Mach wave properties in the presence of source and medium heterogeneity

J. C. Vyas[1], P. M. Mai[1], M. Galis[1,4], Eric M. Dunham[2], and W. Imperatori[3]

[1]King Abdullah University of Science and Technology, [2]Stanford University, [3]Swiss Seismological Service, ETH Zurich, [4]Comenius University, Bratislava.

Email: Jagdish.Vyas@kaust.edu.sa

Summary

We investigate Mach wave coherence for kinematic supershear ruptures with spatially heterogeneous source parameters, embedded in 3D scattering media. We assess Mach wave coherence considering: 1) source heterogeneities in terms of variations in slip, rise time and rupture speed; 2) small-scale heterogeneities in Earth structure, parameterized from combinations of three correlation lengths and two standard deviations (assuming von Karman power spectral density with fixed Hurst exponent); and 3) joint effects of source and medium heterogeneities. Ground-motion simulations are conducted using a generalized finite-difference method, choosing a parameterization such that the highest resolved frequency is ~5 Hz.

We discover that Mach wave coherence is slightly diminished at near fault distances (< 10 km) due to spatially variable slip and rise time; beyond this distance the Mach wave coherence is more strongly reduced by wavefield scattering due to small-scale heterogeneities in Earth structure. Based on our numerical simulations and theoretical considerations we demonstrate that the standard deviation of medium heterogeneities controls the wavefield scattering, rather than the correlation length. In addition, we find that peak ground accelerations in the case of combined source and medium heterogeneities are consistent with empirical ground motion prediction equations for all distances, suggesting that in nature ground shaking amplitudes for supershear ruptures may not be elevated due to complexities in the rupture process and seismic wave-scattering.

Key words: Mach wave; Kinematic rupture; 3D scattering media; Ground motion prediction equations.

1 Introduction

Seismological studies for crustal earthquakes report that the rupture front typically propagates at ~80% of the shear-wave speed (e.g. Heaton, 1990; Mai and Thingbaijam, 2014). However, the rupture speed may exceed the shear wave speed, as shown by theoretical and observational studies. For example, by analyzing strong motion records, it was shown for several earthquakes that the rupture locally propagated faster than the shear-wave speed (Vs) (e.g., for the 1979 M_W 6.5 Imperial Valley, California, earthquake: Olson and Apsel, 1982; Archuleta, 1984; for the 1999 M_W 7.6 Izmit and M_W 7.2 Duzce, Turkey, earthquakes: Bouchon et al., 2001; for the 2002 M_W 7.9 Denali Fault, Alaska, earthquake: Ellsworth et. al., 2004; Aagaard and Heaton, 2004; Dunham and Archuleta, 2004). The analysis of seismic waveforms recorded at regional (< 2000 km) or teleseismic distances demonstrated that the 2001 M_W 7.8 Kunlun, Tibet, earthquake (Walker and Shearer, 2009; Vallee and Dunham, 2012) and the 2013 M_W 7.5 Craig, Alaska, earthquake (Yue et. al., 2013) also showed supershear rupture speed over parts of the fault plane. Both strong motion and teleseismic records suggest that the 2010 M_W 6.9 Qinghai, China, earthquake may have propagated at supershear speed (Wang and Mori, 2012). Therefore, seismic waveforms recorded in the near-field as well as at far-field distances from different earthquakes provide evidence for the existence of supershear ruptures.

Kinematic and dynamic rupture models predict larger ground-motion amplitudes (or high frequencies) from supershear rupture compared to sub-Rayleigh rupture (e.g., Bernard and Baumont, 2005; Dunham and Archuleta, 2005). However, the analytical studies and dynamic rupture modeling show that a crack tip propagating at supershear speed creates a slip velocity function with reduced high-frequency content compared to the sub-Rayleigh case (Andrews, 1976; Bizzarri and Spudich, 2008). Additionally, Bizzarri and Spudich (2008) demonstrate that Mach cone amplification of high frequencies

overwhelms the reduction of high-frequency content in slip velocity for supershear ruptures, leading to a net enhancement of high frequencies for supershear ruptures. Nevertheless, the two competing effects of dynamic reduction of high frequencies in slip velocity and large ground-motion amplitudes for supershear ruptures requires further exploration.

Furthermore, Dunham and Bhat (2008) show that supershear ruptures radiate both shear and Rayleigh Mach waves that transmit large amplitude of ground motions even to large distances from the fault. Andrews (2010) analyzed ground velocities from sub-Rayleigh and supershear events for 2D models with same fracture energy and stress drop. The directivity beam generated in the sub-Rayleigh case is concentrated in a narrow azimuth range around the fault having intense peak velocity, but attenuates as the beam diverges with increasing distance from the fault. The Mach wave from supershear ruptures forms a beam of parallel rays with constant amplitudes out to greater distances, and attenuates due to diffraction and scattering.

In addition to the above findings, Bizzarri et al. (2010) studied the effects of heterogeneous rupture propagation on shear and Rayleigh Mach wave coherence for supershear ruptures on a vertical planar fault embedded in a homogeneous medium. They found that heterogeneous rupture propagation reduces peak ground velocity, but the shear and Rayleigh Mach waves generated by supershear ruptures transmit larger ground motion much farther from the fault compared to sub-Rayleigh ruptures. They utilized strong motion records from three supershear earthquakes to validate their numerical modeling results, investigating spectral acceleration (SA) at stations that presumably experienced Mach waves during the 1979 Imperial Valley, 1999 Izmit, and 2002 Denali Fault earthquakes. Comparing to SA observed at non-Mach-pulse stations for the same earthquake, they found no average elevation of spectral acceleration relative to ground motion prediction equations. This difference could arise either from the sparsity of the data (i.e., supershear ruptures do have larger ground motions, on average, but the few records may have been biased fortuitously toward lower ground motions) or there are additional processes that reduce ground motions from supershear ruptures (e.g., loss of Mach front coherence by additional source complexity and/or scattering along the wave propagation path). The purpose of this study is to

investigate the discrepancy between observations and previous studies through a set of simulations that explicitly take into account small-scale heterogeneities and the resulting wave scattering.

Mach-wave observations are still limited in seismology. Either Mach waves are generally not excited because super-shear rupture propagation occurs only infrequently, or Mach-wave signatures are lost due to seismic-wave propagation effects. Heterogeneities present in the Earth's crust scatter seismic waves, and their impact on ground-motion has been the subject of several numerical studies (Frankel and Clayton, 1986; Frenje and Juhlin, 2000; Pitarka and Ichinose, 2009; Hartzell et al., 2010; Imperatori and Mai, 2013; Bydlon and Dunham, 2015). The effects of seismic scattering are more pronounced on S-waves than P-waves, and mainly distort the S-wave radiation pattern at frequencies above 2 Hz at distances relevant for seismic hazard (Pitarka and Ichinose, 2009; Takemura et al., 2009). In addition, numerical simulations show substantial influence of medium heterogeneities on ground velocities (Hartzell et al., 2010) and ground accelerations (Imperatori and Mai, 2013). Moreover, scattering extends the duration of incoherent high frequency ground-motion and increases the root-mean-square acceleration, at least in 2D (Bydlon and Dunham, 2015). However, these studies focused exclusively on sub-Rayleigh ruptures embedded in heterogeneous media, and hence provide no information on ground motion radiated by supershear ruptures.

To analyze the effects of medium heterogeneity and rupture complexity on Mach wavefront properties, we conduct a set of numerical experiments. We hypothesize that random heterogeneities in Earth structure and rupture complexities diminish or even destroy the coherence of Mach-waves and reduce their high frequency content. We perform ground-motion simulations using kinematic earthquake sources with specified spatio-temporal rupture evolution. The seismic wavefield is computed using a 3D finite-difference method. Wavefield signatures as well as ground-motion parameters are then analyzed with respect to Mach wave effects.

The sections of the paper are organized as follows. First, we describe the computational model geometry and analyze the effects of source heterogeneities on Mach-wave properties. Next, we present

the effects of medium heterogeneities on the seismic wavefield. Finally, we study the combined effects of source and medium heterogeneities on Mach wave.

2 Model geometry and computational method

The section describes the source and medium used as the reference case, receiver geometry, and numerical method employed to compute ground-motions.

2.1 Source model description

We use a kinematic source description that specifies the spatio-temporal evolution of slip in terms of a discrete set of point moment tensor sources. The heterogeneous slip distribution (D) is characterized by a von Karman autocorrelation function (Mai and Beroza, 2002), parameterized by correlation lengths in the along-strike (ax = 16 km) and down-dip (az = 4 km) directions, and Hurst exponent (H = 0.75). Our slip realizations preserve one point statistics as the complementary cumulative distribution function (CCDF) of slip exhibits truncated exponential behavior as observed by Thingbaijam and Mai (2016). The rise time (Tr) and rupture speed (Vr) variations are obtained assuming correlation with slip based on previous studies. Dynamic rupture simulations show 50-70% correlation between slip and rise time (Schmedes et al., 2010; Schmedes et al., 2013; Mai et al., 2017), however, the correlation of slip with rupture velocity is more complex. Some studies considering dynamic rupture models show that faster rupture speed correlates with areas of large slip (Oglesby and Day, 2002; Guatteri et al., 2003), whereas other studies find little or almost no correlation between these two parameters (Schmedes et al., 2010; Mai et al., 2017). In this study, we consider 30% and 60% correlation of rupture speed and rise time, respectively, with slip, consistent with values used by Liu et al. (2006) in their rupture generator.

Correlations among rupture parameters are developed following the theory of Gaussian random variables, similar to previous studies (Liu et al., 2006; Graves and Pitarka, 2016). We generate three (X1, X2 & X3) 2D random fields filtered using von Karman autocorrelation function. Then, from a linear combination of X1 and X2 (or X1 and X3) a new random variable X4 (or X5) is created. Finally, we generate three random fields Y1, Y2 and Y3 using X1, X4 and X5 which are properly scaled and have desired correlation among them. The equations are as follows:

$$X4 = \rho\, X1 + \sqrt{1-\rho^2}\, X2 \text{ and } X5 = \rho\, X1 + \sqrt{1-\rho^2}\, X3 \quad (1)$$

where ρ is the correlation coefficient, and

$$Y1 = \mu_1 + \sigma_1\, X1;\ Y2 = \mu_2 + \sigma_2\, X4;\ Y3 = \mu_3 + \sigma_3\, X5 \quad (2)$$

where (μ_1, σ_1), (μ_2, σ_2), (μ_3, σ_3) are mean and standard deviations of variables X1, X2, X3 respectively. The new random variables Y1, Y2 and Y3 correspond to slip, rise time and rupture speed, respectively, having the desired correlation between Y1 and Y2 (nearly 0.6), and Y1 and Y3 (nearly 0.3) .

We consider a 50 km long and 15 km wide strike-slip fault on which an earthquake occurs of seismic moment 2.8×10^{19} Nm (Mw = 6.9). Figure 1-a show spatial variations of slip, rise time and rupture speed on the fault plane. Note that the rupture parameters are cosine tapered (slip and rupture speed are decreased, whereas rise time is increased) towards the right edge of the fault to weaken the amplitude of stopping phase. In the case of earthquakes with supershear rupture speed, the rupture front initially propagates at a sub-Rayleigh velocity, but then transitions to supershear speed. Therefore, we assume that an unmodeled sub-Rayleigh rupture front arrives from some distance, and then transitions to super-shear speed propagation on the modeled fault area (50 km x 15 km). Correspondingly, rupture onset times on the modeled portion of the fault delineate an almost vertical rupture front (Figure 1-a). The location of minimum rupture onset time denotes the hypocenter (black star). Figure 1-b compares the CCDF of slip against three theoretical functions including lognormal, exponential and truncated exponential to examine the one point statistics. Our slip realizations are in proximity to truncated exponential behaviour. Figure 1-(c,d,e) delineate the correlation among rupture parameters with a linear least squares fit to the data. The

strongest correlation exists between slip and rise time (nearly 60%) compared to other pairs of rupture parameters. The temporal slip-rate evolution at each source point is described by the regularized Yoffe function (Tinti et al., 2005) with fixed acceleration time (τ_{acc} = 0.2 s). We used constant τ_{acc} as the current observational constraints on it, though poor, indicate that τ_{acc} varies only weakly (Tinti et al., 2005). Strike and dip are 90°, and the rake is uniformly set to 0° (left-lateral strike-slip).

We first generate five models having all the parameters heterogeneous (slip, rise time and rupture speed) denoted as MOD-I (I = 1, 2, 3, 4, 5). Figure 1 shows MOD-1, the other four models are shown in Figure S1 of the electronic supplement. We then create a set of 31 rupture models by combining heterogeneous and uniform rupture parameters (Table 1), in which the uniform values are chosen as the corresponding average slip (1.16 m), rise time (1.80 s), and rupture speed (1.57Vs). We refer to the models using their heterogeneous parameters, e.g., MOD-1; H_{Vr} denotes the model created from MOD-1 with heterogeneous (H) rupture speed (Vr), but uniform slip and rise time. Similarly, MOD-2; H_{DTr} indicates source generated using MOD-2 having heterogeneous slip (D) and rise time (Tr), but uniform rupture speed. We also define a reference rupture model with uniform parameters (U_{DTrVr}); thus, we consider in total thirty-six source models.

2.2 Receiver geometry and reference medium

Supershear ruptures propagating at constant rupture velocity Vr generate a planar shear Mach wave that is radiated off the fault at an angle θ (e.g., Bizzarri et al., 2010):

$$\theta = \sin^{-1}\left(\frac{Vs}{Vr}\right) \quad (3)$$

Using Eq. 3, we compute the spatial limits in which the Mach waves travel for average rupture speed (Figure 1f; Vr = 1.57Vs). For our analysis, we examine simulated ground-motions at lines of receivers within the theoretical Mach region boundaries (Figure 1f), but ignore stations at the right end of these boundaries as they are affected by stopping phases. Receivers are spaced at 0.5 km in fault-parallel and 5

km in fault-normal directions. Five additional locations (s1 to s5, Fig. 1f) are used to investigate waveform differences for receivers inside and outside the Mach boundaries.

2.3 Computation of synthetic seismograms

We use the Support Operator Rupture Dynamics (SORD) code, which is a second-order accurate (in space and time) generalized finite-difference solver of the elastodynamic equations (Ely et al., 2008). The reference medium is a homogeneous half-space of uniform S-wave speed (3464 m/s), P-wave speed (6000 m/s), and density (2700 kg/m^3), to which random velocity and density perturbations are added for studying scattering effects (Section 4). The kinematic source is embedded as a point-cloud of local slip-rate functions over the designated rupture area. We use 12-points for the shortest wavelengths at a grid spacing of dx = 50 m, hence the maximum resolved frequency is 5 Hz (to remove unresolved frequencies from the analysis, the resulting seismograms are low-pass filtered using a fourth-order Butterworth filter). The corresponding computational time step (dt = 0.0045 s) is set to satisfy the numerical stability criteria (e.g., Ely et al., 2008).

3 Effect of heterogeneous source parameters

We investigate simulated ground motions with Mach front signatures for the heterogeneous source models, and compare those to waveforms for the uniform reference source. These thirty-six simulations are run using the homogeneous medium and identical receiver geometry to focus on source effects only.

3.1 Synthetic seismograms and wavefield snapshots

Figure 2 compares fault-parallel (FP), fault-normal (FN), and vertical (Ver) components of ground acceleration for source MOD-1 and the reference source U_{DTrVr} at stations s1 - s5 (Fig. 1f; recall that s1, s2 and s3 are within the Mach boundary, s4 and s5 are outside). Sites s3 and s2 clearly show the S-Mach-wave and Rayleigh-Mach-wave, while at site s1 there is no clear separation between the two. The Rayleigh-Mach-wave is most strongly developed on the vertical component, while the S Mach wave is only expressed on the horizontal components. The overall horizontal-component Mach-wave amplitudes from MOD-1 are smaller than from U_{DTrVr}, especially close to the fault (sites s1 and s2), illustrating the effects of rupture parameter heterogeneities. For both sources, site s4 shows significantly lower ground acceleration than site s3 (~8 times on the fault-normal, and ~25 times on the vertical component), although s4 is closer to the fault than s3. Site s5 is located in the direction of rupture propagation, and hence experiences a strong stopping phase arrival before the S-wave, whereas s4 does not (because it is located in the opposite direction). The ground-velocity amplitudes for sources MOD-1 and U_{DTrVr} at these two sites show similar characteristics (Figure S2), indicating larger ground-motions for locations inside the Mach boundaries than outside.

Figure 3 displays snapshots of ground acceleration for source models U_{DTrVr} and MOD-1, illustrating the planar Mach waves due to supershear rupture propagation and a strong stopping phase from sudden rupture arrest at the right fault edge (nicely seen on fault-parallel at 12s and beyond). The fault-parallel and fault-normal components both show the S-Mach-wave and Rayleigh-Mach-wave, while the vertical component only contains the Rayleigh-Mach-wave. Mach-wave amplitudes almost remain unchanged as the waves propagate, even at larger distance from the fault due to their planar nature (perfect planar in 2D and more complex in 3D). The wavefield of ground velocity exhibits similar Mach-wave characteristics as the acceleration wavefield (Figure S3); for both sources, Mach waves travel large distances without significant attenuation. However, Mach wave velocity/acceleration amplitudes are smaller for model MOD-1 than for the reference source $U_{DTrVr.}$

3.2 Peak ground acceleration (PGA)

To further quantify ground-motion characteristics due to the effects of source complexity on Mach wave coherence, we calculate peak ground acceleration (PGA) of the two horizontal components using GMRotD50 method (Boore et al., 2006; calculated by stepwise rotating the two orthogonal horizontal components by 1° increments from 1° to 90°, computing the geometric mean for each pair, and taking PGA as the median of 90 geometric means).

We examine mean and standard deviation of PGA computed using all stations for a given fault-perpendicular distance for the thirty-six models. Figure 4-a compares PGA values for six source models (five sources having D, Tr and Vr heterogeneous; and reference source) as function of distance, showing also the PGA-estimates using the GMPE of Boore and Atkinson (henceforth BA2008). The mean PGA values computed using six sources fall outside the 1-sigma bounds of BA2008 at distances of 10 km and beyond. However, at a distance of 5 km the PGA estimates from the GMPE and our simulations are comparable. At this distance, rupture parameter heterogeneity seems to exert strong effects on ground-shaking (notice the variations of mean PGA, for MOD-1 being lowest to MOD-2 being highest). The overprediction of the simulated PGA values at larger distances is likely due to the omission of scattering in these simulations. The mean PGA for U_{DTrVr} remains almost constant with distance, because the planar Mach wave has negligible attenuation over the modeled distances. Figure 4-b compares PGA values for five source models with only heterogeneous rise time to the reference source and BA2008. The rupture models with only Tr heterogeneous are comparable/lower (but not higher) than reference source. The PGA comparisons for source models having heterogeneities only in D, or Vr, or (D, Tr), or (D, Vr), or (Tr, Vr) are shown in Figure S4 of the electronic supplement.

To further summarize the results, we compute mean and standard deviation of PGAs from five realizations sharing the same rupture parameter heterogeneity and using all stations for a given fault-perpendicular distance. For example, we use PGAs from the five realizations MOD-1, 2, 3, 4, 5; H_{Tr} (five different curves in Figure 4-b), and all receivers at a given distance to obtain the average estimate (a

single representative mean curve of those five curves) denoted as $(H_{Tr})_{avg}$. We use abbreviations $(H_D)_{avg}$, $(H_{Tr})_{avg}$, $(H_{Vr})_{avg}$, $(H_{DTr})_{avg}$, $(H_{DVr})_{avg}$, $(H_{TrVr})_{avg}$, $(H_{DTrVr})_{avg}$ to refer to the averages over five realizations considering heterogeneities only in D, or Tr, or Vr, or (D, Tr), or (D, Vr), or (Tr, Vr), or (D, Tr, Vr) respectively. Figure 4-(c,d) compares PGA estimates calculated by averaging over five realizations for a given kind of heterogeneity to the reference source and BA2008. The PGAs from $(H_D)_{avg}$, $(H_{Tr})_{avg}$, and $(H_{DTr})_{avg}$ are comparable/lower (but not higher) than the U_{DTrVr} for all distances, with $(H_{DTr})_{avg}$ being the lowest indicates that both slip and rise time heterogeneities slightly reduce the Mach-wave coherence. The physical explanation could be that the peak slip velocity (PSV) dominantly controls the peak ground-motion, and PSV is mainly controlled by slip and rise time for fixed acceleration time. In general, we observe that the source rise time and slip heterogeneities slightly lower the PGA values from supershear ruptures in near-fault distances ($\leq$ 10 km).

3.3 Average Fourier Acceleration (AFA)

To investigate the spectral characteristics of the seismic wavefield, we calculate Fourier spectra of unfiltered acceleration time series at each site. We then compute the average Fourier acceleration (AFA) as the mean of the spectra for multiple sites at a given distance from the fault. Figure 5 compares AFA for the fault-parallel and fault-normal components for the six sources. The variations in AFAs for MOD-1, 2, 3, 4, 5 compared to U_{DTrVr} at 5 km distance depicts the effects of rupture parameter heterogeneity on frequency content of ground-motions generated from supershear ruptures. At larger distances (>= 20 km), the variations among the AFAs are lower compared to a distance of 5 km. The AFAs for sources having heterogeneity only in rise time show less fluctuations compared to rupture models having heterogeneity in all parameters (compare Figure 5 with Figure S5 of electronic supplement).

4 Effects of scattering medium

We now investigate the effects of seismic scattering on Mach-wave characteristics by computing the seismic wavefield for U_{DTrVr} embedded into realizations of heterogeneous 3D Earth media. The resulting ground-motions are analyzed analogous to the homogeneous-medium case.

4.1 Realization of 3D random media

Small-scale heterogeneities in Earth structure cause seismic scattering that leads to wave-front distortion, redistribution of wave energy, and pronounced changes of seismic waveforms. Frankel and Clayton (1986) studied scattering of elastic and acoustic waves in 2D random media characterized by variations in seismic wave speeds. They considered three different correlation functions (Gaussian, exponential, and self-similar von Karman), and observed that 2D self-similar random media with 5% velocity fluctuations and correlation lengths of 10 km (or greater) may explain travel-time anomalies across seismic arrays and the coda waves of micro earthquakes. Ritter et al. (1998) analyzed teleseismic P-wave recordings to determine scattering-media parameters of the lithosphere. For their study region (central France), they proposed a model of the lithosphere consisting of a heterogeneous layer of 70 km thickness with correlations lengths of 1 – 16 km and velocity fluctuations of 3 – 7%. These values are in agreement with Rothert and Ritter (2000) who determine the small-scale heterogeneous structure of the upper lithosphere beneath the Grafenberg array, Germany, and find wave-speed perturbations of 3 – 7% and correlation lengths of 0.6 – 4.8 km.

We introduce small-scale heterogeneities into a homogeneous background model by adding a spatial random field, characterized by an isotropic von Karman autocorrelation function, following the approach of Imperatori and Mai (2013). The power spectral density of the von Karman function is described as,

$$p(k) = \frac{\sigma^2 (2\sqrt{\pi}a)^3 \Gamma(H+1.5)}{\Gamma(H) (1+k^2a^2)^{(H+1.5)}} \quad (4)$$

where a, H, σ, k, and r are correlation length, Hurst exponent, standard deviation, wave number, and the Gamma function, respectively. We generate six realizations of the 3D random field using three correlation lengths (5.0 km, 2.0 km, 0.5 km), and two standard deviations (5%, 10%) for fixed Hurst exponent (H = 0.2). The choice of these parameters values is motivated by data analysis using borehole logs and seismic reflection data (e.g., Dolan and Bean 1997; Bean et. al., 1999). The six realizations of randomized 3D Earth models (having variations in velocity as well as density) are referred to as M1 to M6 (Table 2), shown in terms of surface slices of S-wave speed to illustrate the effects of different correlation lengths and standard deviations (Figure 6).

We place the reference source U_{DTrVr} in six different random media, and conduct ground motion simulations for the same receiver geometry as before. Due to regions of lower shear-wave speeds in these random-media realizations, we have to reduce the spatial grid size to dx = 25 m, and the computational time steps to dt = 0.0018 s and dt = 0.0014 s for media with standard deviations of 5% and 10%, respectively.

4.2 Synthetic seismograms and wavefield snapshots

Figure 7 compares fault-parallel, fault-normal, and vertical components of ground acceleration at sites s1 to s5 (Fig 1f) for M1 (a = 5.0 km, σ = 5%) and M4 (a = 5.0 km, σ = 10%) with the homogeneous-medium case, using the uniform source model. S-wave Mach amplitudes at station s1 on the fault-parallel and fault-normal components are smaller for M4 than for the homogeneous medium. As the S-Mach waves propagate away from the fault, amplitudes are further reduced for M4 compared to the homogeneous medium due to the cumulative effects of seismic scattering. The S-Mach wave amplitudes at sites s2 and s3 for M4 are comparable to scattered-wavefield amplitudes arriving after the S-Mach wave, suggesting that medium scattering may potentially obfuscate Mach-wave detection in real

earthquakes. Scattering of the S-wave Mach waves is stronger for M4 than for M1, due to the higher standard deviation of the random wave-speed fluctuations. Sites outside the Mach boundaries (s4 and s5) also experience larger scattering for M4 than M1. Rayleigh-Mach-waves on the vertical components of s1 and s2 have comparable amplitudes for all three media, but have smaller amplitude at site s3 for media M4 and M1 compared to the homogeneous medium. Ground-motion velocities at the five stations s1 to s5 for media M1 and M4 exhibit generally similar scattering effects as seen in ground acceleration (Figure S6). In general, Mach-wave amplitudes are reduced in media with small-scale random heterogeneities (especially for $\sigma = 10\%$), compared to the homogeneous medium, since the elastic scattering redistributes the wave energy in space and time.

Figure 8 shows snapshots of ground-motion acceleration at different times for media M1 ($a = 5.0$ km, $\sigma = 5\%$) and M4 ($a = 5.0$ km, $\sigma = 10\%$). The corresponding snapshots of ground velocity are provided in Figure S7, but seismic scattering is more prominently visible in the acceleration wavefield. As the Mach wave travels away from the fault, its amplitude decreases and its coherence is reduced. In fact, the scattering effects are so strong for M4 that the plane-wave structure of the Mach wave is difficult to identify after 9 s. In addition, the amplitudes of the scattered wavefield and the Mach wave become comparable (as seen already on seismograms s1 to s3).

4.3 Peak ground acceleration (PGA)

Following our previous approach, we quantify the effects of seismic scattering in heterogeneous media using PGA values as a ground-motion intensity measure. Figure 9 displays PGA values for the six scattering media M1-M6 and the homogeneous medium for simulations with the uniform source model; PGA computed using BA2008 facilitates the comparison. The mismatch between GMPE-estimates and simulations can partially be attributed to the absence of rupture complexity in these simulations. Mean PGA values for M1 and M2 ($\sigma = 5\%$) are near or just outside the 1-sigma bound of BA2008 for all distances, while mean PGA for M4 and M5 ($\sigma = 10\%$) are within the 1-sigma bound of BA2008. For

distances larger ~10 km, mean PGA values from BA2008 and our simulations begin to converge. The standard deviation of medium heterogeneities seems to control the seismic scattering rather than correlation length for small H (≤ 0.2). The wavefield scattering for medium M3 is smaller than M1 and M2 as the correlation length of 0.5 km is smaller than the minimum physical wavelength corresponding to background homogeneous medium (3.464/5 ~ 0.7 km). Due to the same reason, M6 show lower mach wave scattering compared to M4 and M5. In summary, we find that seismic scattering due to small-scale random heterogeneities in the Earth destroys the coherence of Mach waves, and thus complicates their observation in nature.

4.4 Average Fourier Acceleration (AFA)

We examine the spectral characteristic of scattered Mach waves by comparing AFA spectra computed as mean amplitude spectra for stations at a given distance from the fault. Figure 10 depicts AFA spectra as a function of frequency for the horizontal components of motion for the homogeneous and six heterogeneous media. All AFA spectra are similar, on both components, at 5 km distance, showing that scattering is relatively unimportant at these close distances. With increasing distance, AFA spectra for scattering media decrease more rapidly than for the homogeneous medium, at all frequencies above 1 Hz, due to the cumulative nature of scattering effects. We also observe that AFA spectra for M4, M5, and M6 (σ = 10%) decrease more rapidly than for M1, M2, and M3 (σ = 5%), indicating that seismic scattering is controlled by the standard deviation of the velocity fluctuations.

5 Effects of combined source and medium heterogeneities

Mach wave coherence is affected by slip and rise time heterogeneities at close fault distances (< 10 km), whereas the influence of seismic scattering becomes dominant beyond larger distances (> 10 km). However, in nature all rupture parameters are most likely heterogeneous (D, Tr and Vr), therefore, we

choose MOD-1 and MOD-2 (also end members in terms of mean PGA at 5 km distance, see Figure 4-a) as representative heterogeneous rupture models. We select random medium M4 as an end member medium due to its strongest impact on Mach waves (see Section 4). Now, we combine both source and medium heterogeneities to examine their overall effects on the Mach wave. We then analyze the synthetic ground-motions at several receivers like in Sections 3 and 4.

5.1 Synthetic seismograms and wavefield snapshots

Figure 11 compares fault-parallel, fault-normal, and vertical components of ground acceleration from MOD-1 in M4 to U_{DTrVr} in a homogeneous-medium at locations s1-s5. The S-Mach wave amplitudes on fault-parallel and fault-normal at s1 are now even smaller, because of the combined source and medium heterogeneities, compared to considering each case individually (compare Fig. 11 with Figs. 2 and 7). The Rayleigh-Mach wave amplitudes on the vertical component are lower for MOD-1 in M4 than in the reference case at station s3, but are comparable at sites s1 and s2. Therefore, they are mostly affected by medium heterogeneities, while the source heterogeneities have smaller effects. The particle velocities are also lower at stations s1 and s3 for MOD-1 in M4 than in the reference case, whereas comparable at s2 (electronic supplement, Figure S8).

The fault-parallel, fault-normal, and vertical components of ground-acceleration (Figure 12) and ground velocity (electronic supplement, Figure S9) are displayed for MOD-1 in M4. The scattering effects are more prominent in the acceleration wavefield compared to velocity wavefield. Nevertheless, the planar structure of the Mach pulse is harder to recognize in acceleration/velocity snapshots at 9 s and beyond.

5.2 Peak ground acceleration (PGA)

We apply the same approach as before and compute PGA to examine the effects of combined source and medium heterogeneities. Figure 13 compares PGA values from MOD-1 and MOD-2 in M4 to U_{DTrVr} in the homogeneous medium. The PGA from BA2008 are plotted to facilitate comparisons. The mean PGA values from MOD-1 and MOD-2 in M4 are comparable to BA2008 (MOD-1 in M4 being closer), whereas those from U_{DTrVr} in the homogeneous medium remain significantly higher. The physical explanation is the presence of source effects in the near-field (< 10 km), while medium scattering effects are dominant only at larger distances (> 10 km), leading to overall diminished Mach wave amplitude at all distances. Additionally, the PGA at stations s4 and s5 (which are outside the theoretical Mach cone boundary) for MOD-1 in M4 are within the one-sigma bounds of BA2008, indicating that our choices for source and medium parameterizations are reasonable. Moreover, we check the effects of intrinsic attenuation on PGA levels from MOD-1 in M4. We apply Futterman filter (e.g. Varela et al., 1993) which depends on Q and travel time as post-processing to the synthetic waveforms. We adopt a constant Q value of 350 (~Vs/10) following Chandler et al. (2006). We observe negligible reduction in PGA (~ 0.2%) due to intrinsic attenuation for MOD-1 in M4, and therefore, its not shown in Figure 13.

Overall, we find that for scenarios with combined source and medium heterogeneities, the Mach wave coherence is strongly reduced, which in turn leads to the effect that PGA-levels are not elevated when compared to a GMPE. Therefore, source and medium complexity destroy the theoretically expected stronger shaking for supershear ruptures.

5.3 Average Fourier Acceleration (AFA)

Figure 14 illustrates the AFA for fault-parallel and fault-normal components of ground acceleration for MOD-1, 2 in M4 and U_{DTrVr} in the homogeneous medium. The AFA for MOD-1 in random medium M4 is close to U_{DTrVr} in homogeneous medium at 5 km distance. The source effects are masked by medium scattering already at 5 km distance; otherwise, lower AFA is expected for MOD-1 in the homogeneous medium (see Figure 5). The AFA for MOD-2 in M4 is higher than U_{DTrVr} at 5 km

distance due to the dominance of source effects as previously observed for MOD-2 in homogeneous medium (see Figure 5). The AFA decreases with increasing distance for MOD-1, 2 in M4 faster than the reference case beyond 1 Hz, but the decline from combined source and medium heterogeneities is comparable to what is seen in the case of medium heterogeneities only (compare Figure 14 with Figure 10). At 35 km (and beyond), the AFA from MOD-2 in M4 approaches MOD-1 in M4. Overall, we find that heterogeneities in source and medium collectively lead to lowered AFA from supershear ruptures within the Mach cone region.

6 Discussion

The ground-shaking computed by considering variations only in source parameters illustrate that slip and rise time variability slightly lowers the Mach wave coherence in near fault distances (< 10 km). Bizzarri et al. (2010) investigated the effects of rupture complexity on Mach waves, arising from heterogeneities in initial shear stress in their dynamic source models. They observed reduced peak ground velocity (PGV) due to variations of rupture speed and spatially less correlated slip velocity time histories. Similarly, we also notice nearly 10% decrease of PGA (due to $(H_{DTr})_{avg}$) in close distances to the fault (< 10 km). Some of the differences (in terms of PGA decrease) could arise between the two studies due to large slip-weakening distances used by Bizzarri et al (2010), which may weaken the effects of stress heterogeneities. Their Fourier amplitude spectrum ratio between homogeneous and heterogeneous supershear rupture is nearly one. In contrast, we find a decline/increase of the average Fourier amplitudes for MOD-1/MOD-2 compared to U_{DTrVr}, indicating a significant effect of source complexity on the spectral ratios at short distances (< = 5 km).

Mach wave coherence beyond 10 km distance is reduced due to wavefield scattering from small-scale heterogeneities in the Earth. Bydlon and Dunham (2015) show that seismic scattering increases the duration of incoherent high frequencies, and hence elevates the root-mean-square acceleration, at least in

2D. However, the Mach pulse is an extremely coherent high-frequency seismic wave, therefore, scattering lowers the PGA by redistributing the frequencies in the entire 3D medium. Imperatori and Mai (2013) observe PGA decrease with increasing epicentral distance as a result of wavefield scattering for sub-Rayleigh ruptures. This supports our finding of medium scattering being responsible for the decline of Mach front coherence at large distances (> 10 km) for supershear ruptures.

Ground-shaking levels in terms of PGA from supershear ruptures (in the Mach cone region) with both medium and source heterogeneities are in overall agreement with BA2008. The GMPEs inherently include intrinsic attenuation, whereas our simulations are elastic and we only approximately check for attenuation in a post-processing step (assuming constant Q); however, detailed consideration of anelastic attenuation may slightly reduce the shaking levels. Overall, we discover that the Mach wave coherence is slightly lowered by variations in slip and rise time in close distances to the fault (< 10 km) and beyond this distance the wavefield scattering reduces the Mach wave coherence more dominantly resulting in PGAs from supershear ruptures comparable to BA2008. Therefore, our findings explain the observation of Bizzarri et al. (2010) that spectral accelerations (SA) were not elevated at stations that experienced Mach waves, compared to stations unaffected by the Mach pulse, during the 1979 Imperial Valley, 1999 Izmit, and 2002 Denali Fault earthquakes.

Our simulations are kinematic, in order to be able to precisely control the rupture complexity and the occurrence and spatial extent of supershear propagation. Thus, we do not attempt to study when and why supershear rupture happens. Additionally, Vyas et al. (2016) found that the ground-motion variability is higher than BA2008 in close distances to the fault (< 20 km) at least for subshear ruptures considering heterogeneous rupture on the faults having geometric complexity. Therefore, dynamic simulations with large-scale fault segmentation and/or small-scale fault roughness are required, which may provide more insight into rupture heterogeneity and ground-motion complexity from supershear earthquakes. Fault segmentation may control rupture nucleation, rupture arrest, and the seismic moment release for sub-Rayleigh speeds (Oglesby and Mai, 2012; Aochi and Ulrich, 2015). Fault roughness causes localized acceleration/deceleration of the rupture front due to local stress perturbations leading to

high frequency radiation (Madariaga, 1977; Dunham et al., 2011; Shi and Day, 2013) that is important for engineering purposes and seismic-hazard estimation. Therefore, dynamic simulations with realistic variations in initial stress, friction on the fault, off-fault plasticity, 3D medium heterogeneities, non-planar fault geometry, and fault roughness are needed to gain a deeper understanding of the Mach wave coherence and resulting ground-shaking properties.

7 Conclusions

Ground-motion simulations reveal that Mach wave coherence is slightly diminished in the near-field of earthquake rupture (distance < 10 km) by spatial variations of rise time and slip, while wavefield scattering reduces coherence more dominantly at larger distances (> 10 km). Theory predicts larger ground-motion amplitudes and higher frequency content for supershear than sub-Rayleigh ruptures, whereas PGAs from our simulations (MOD-1 and MOD-2 in M4) are almost consistent with BA2008. We speculate that local supershear ruptures might be more common in nature than reported, but not easily detectable due to wavefield scattering and rupture complexity.

8 Acknowledgements

We thank the editor Jean Virieux and the two anonymous reviewers for their constructive critical review that helped us to improve the manuscript. The research presented in this article is supported by King Abdullah University of Science and Technology (KAUST) in Thuwal, Saudi Arabia, grants BAS/1/1339-01-01 and AEA-7000000083. Earthquake rupture and ground-motion simulations have been carried out using the KAUST Supercomputing Laboratory (KSL), and we acknowledge the support of the KSL staff. Walter Imperatori was supported through a contract with the Swiss Federal Nuclear Safety Inspectorate (ENSI).

References

Aagaard, B. T., & Heaton, T. H. (2004). Near-source ground motions from simulations of sustained intersonic and supersonic fault ruptures. Bulletin of the Seismological Society of America, 94(6), 2064-2078.

Andrews, D. J. (1976). Rupture velocity of plane strain shear cracks. Journal of Geophysical Research, 81(32), 5679-5687.

Andrews, D. J. (2010). Ground motion hazard from supershear rupture. Tectonophysics, 493(3), 216-221.

Aochi, H., & Ulrich, T. (2015). A probable earthquake scenario near Istanbul determined from dynamic simulations. Bulletin of the Seismological Society of America, 105(3), 1468-1475.

Archuleta, R. J. (1984). A faulting model for the 1979 Imperial Valley earthquake. J. geophys. Res, 89(6), 4559-4585.

Bean, C. J., Marsan, D., & Martini, F. (1999). Statistical Measures of Crustal Heterogeneity from Reflection Seismic Data: The Role of Seismic Bandwidth. Geophysical Research Letters, 26(21), 3241-3244.

Bernard, P., & Baumont, D. (2005). Shear Mach wave characterization for kinematic fault rupture models with constant supershear rupture velocity. Geophysical Journal International, 162(2), 431-447.

Bizzarri, A., & Spudich, P. (2008). Effects of supershear rupture speed on the high-frequency content of S waves investigated using spontaneous dynamic rupture models and isochrone theory. Journal of Geophysical Research: Solid Earth, 113(B5).

Bizzarri, A., Dunham, E. M., & Spudich, P. (2010). Coherence of Mach fronts during heterogeneous supershear earthquake rupture propagation: Simulations and comparison with observations. Journal of Geophysical Research: Solid Earth, 115(B8).

Boore, D. M., & Atkinson, G. M. (2008). Ground-motion prediction equations for the average horizontal component of PGA, PGV, and 5%-damped PSA at spectral periods between 0.01 s and 10.0 s. Earthquake Spectra, 24(1), 99-138.

Boore, D. M., Watson-Lamprey, J., & Abrahamson, N. A. (2006). Orientation-independent measures of ground motion. Bulletin of the seismological Society of America, 96(4A), 1502-1511.

Bouchon, M., Bouin, M. P., Karabulut, H., Toksöz, M. N., Dietrich, M., & Rosakis, A. J. (2001). How fast is rupture during an earthquake? New insights from the 1999 Turkey earthquakes. Geophysical Research Letters, 28(14), 2723-2726.

Bydlon, S. A., & Dunham, E. M. (2015). Rupture dynamics and ground motions from earthquakes in 2-D heterogeneous media. Geophysical Research Letters, 42(6), 1701-1709.

Chandler, A. M., Lam, N. T. K., & Tsang, H. H. (2006). Near-surface attenuation modelling based on rock shear-wave velocity profile. Soil Dynamics and Earthquake Engineering, 26(11), 1004-1014.

Dolan, S. S., & Bean, C. J. (1997). Some remarks on the estimation of fractal scaling parameters from borehole wire-line logs. Geophysical Research Letters, 24(10), 1271-1274.

Dunham, E. M., & Archuleta, R. J. (2004). Evidence for a supershear transient during the 2002 Denali fault earthquake. Bulletin of the Seismological Society of America, 94(6B), S256-S268.

Dunham, E. M., & Archuleta, R. J. (2005). Near-source ground motion from steady state dynamic rupture pulses. Geophysical Research Letters, 32(3).

Dunham, E. M., & Bhat, H. S. (2008). Attenuation of radiated ground motion and stresses from three-dimensional supershear ruptures. Journal of Geophysical Research: Solid Earth, 113(B8).

Dunham, E. M., Belanger, D., Cong, L., & Kozdon, J. E. (2011). Earthquake ruptures with strongly rate-weakening friction and off-fault plasticity, Part 2: Nonplanar faults. Bulletin of the Seismological Society of America, 101(5), 2308-2322.

Ellsworth, W. L., Celebi, M., Evans, J. R., Jensen, E. G., Kayen, R., Metz, M. C., ... & Stephens, C. D. (2004). Near-field ground motion of the 2002 Denali Fault, Alaska, earthquake recorded at Pump Station 10. Earthquake Spectra, 20(3), 597-615.

Ely, G. P., Day, S. M., & Minster, J. B. (2008). A support-operator method for viscoelastic wave modelling in 3-D heterogeneous media. Geophysical Journal International, 172(1), 331-344.

Frankel, A., & Clayton, R. W. (1986). Finite difference simulations of seismic scattering: Implications for the propagation of short-period seismic waves in the crust and models of crustal heterogeneity. Journal of Geophysical Research: Solid Earth, 91(B6), 6465-6489.

Frenje, L., & Juhlin, C. (2000). Scattering attenuation: 2-D and 3-D finite difference simulations vs. theory. Journal of applied geophysics, 44(1), 33-46.

Graves, R., & Pitarka, A. (2016). Kinematic ground-motion simulations on rough faults including effects of 3D stochastic velocity perturbations. Bulletin of the Seismological Society of America, 106(5), 2136-2153.

Guatteri, M., Mai, P. M., Beroza, G. C., & Boatwright, J. (2003). Strong ground-motion prediction from stochastic-dynamic source models. Bulletin of the Seismological Society of America, 93(1), 301-313.

Hartzell, S., Harmsen, S., & Frankel, A. (2010). Effects of 3D random correlated velocity perturbations on predicted ground motions. Bulletin of the Seismological Society of America, 100(4), 1415-1426.

Heaton, T. H. (1990). Evidence for and implications of self-healing pulses of slip in earthquake rupture. Physics of the Earth and Planetary Interiors, 64(1), 1-20.

Imperatori, W., and Mai P. M. (2013). Broad-band near-field ground motion simulations in 3-dimensional scattering media, Geophys. J. Int. 192, no. 2, 725–744.

Liu, P., Archuleta, R. J., & Hartzell, S. H. (2006). Prediction of broadband ground-motion time histories: Hybrid low/high-frequency method with correlated random source parameters. Bulletin of the Seismological Society of America, 96(6), 2118-2130.

Madariaga, R. (1977). High-frequency radiation from crack (stress drop) models of earthquake faulting. Geophysical Journal International, 51(3), 625-651.

Mai, P. M., & Beroza, G. C. (2002). A spatial random field model to characterize complexity in earthquake slip. Journal of Geophysical Research: Solid Earth, 107(B11).

Mai, P. M., & Thingbaijam, K. K. S. (2014). SRCMOD: An online database of finite-fault rupture models. Seismological Research Letters, 85(6), 1348-1357.

Mai, P. M., Galis, M., Thingbaijam, K. K., Vyas, J. C., & Dunham, E. M. (2017). Accounting for fault roughness in pseudo-dynamic ground-motion simulations. Pure and Applied Geophysics, 174(9), 3419-3450.

Oglesby, D. D., & Day, S. M. (2002). Stochastic fault stress: Implications for fault dynamics and ground motion. Bulletin of the Seismological Society of America, 92(8), 3006-3021.

Oglesby, D. D., & Mai, P. M. (2012). Fault geometry, rupture dynamics and ground motion from potential earthquakes on the North Anatolian Fault under the Sea of Marmara. Geophysical Journal International, 188(3), 1071-1087.

Olson, A. H., & Apsel, R. J. (1982). Finite faults and inverse theory with applications to the 1979 Imperial Valley earthquake. Bulletin of the Seismological Society of America, 72(6A), 1969-2001.

Pitarka, A., & Ichinose, G. (2009). Simulating forward and backward scattering in viscoelastic 3D media with random velocity variations and basin structure. US Geol. Surv. Tech. Rep.

Ritter, J. R., Shapiro, S. A., & Schechinger, B. (1998). Scattering parameters of the lithosphere below the Massif Central, France, from teleseismic wavefield records. Geophysical Journal International, 134(1), 187-198.

Rothert, E., & Ritter, J. R. (2000). Small-scale heterogeneities below the Gräfenberg array, Germany from seismic wavefield fluctuations of Hindu Kush events. Geophysical Journal International, 140(1), 175-184.

Schmedes, J., Archuleta, R. J., & Lavallée, D. (2010). Correlation of earthquake source parameters inferred from dynamic rupture simulations. Journal of Geophysical Research, 115(B3), B03304.

Schmedes, J., Archuleta, R. J., & Lavallée, D. (2013). A kinematic rupture model generator incorporating spatial interdependency of earthquake source parameters. Geophysical Journal International, 192(3), 1116-1131.

Shi, Z., & Day, S. M. (2013). Rupture dynamics and ground motion from 3-D rough-fault simulations. Journal of Geophysical Research: Solid Earth, 118(3), 1122-1141.

Takemura, S., Furumura, T., & Saito, T. (2009). Distortion of the apparent S-wave radiation pattern in the high-frequency wavefield: Tottori-Ken Seibu, Japan, earthquake of 2000. Geophysical Journal International, 178(2), 950-961.

Thingbaijam, K. K., & Martin Mai, P. (2016). Evidence for truncated exponential probability distribution of earthquake slip. Bulletin of the Seismological Society of America, 106(4), 1802-1816.

Tinti, E., Fukuyama, E., Piatanesi, A., & Cocco, M. (2005). A kinematic source-time function compatible with earthquake dynamics. Bulletin of the Seismological Society of America, 95(4), 1211-1223.

Vallée, M., & Dunham, E. M. (2012). Observation of far-field Mach waves generated by the 2001 Kokoxili supershear earthquake. Geophysical Research Letters, 39(5).

Varela, C. L., Rosa, A. L., & Ulrych, T. J. (1993). Modeling of attenuation and dispersion. Geophysics, 58(8), 1167-1173.

Vyas, J. C., Mai, P. M., & Galis, M. (2016). Distance and azimuthal dependence of ground-motion variability for unilateral strike-slip ruptures. Bulletin of the Seismological Society of America, 106(4), 1584-1599.

Walker, K. T., & Shearer, P. M. (2009). Illuminating the near-sonic rupture velocities of the intracontinental Kokoxili Mw 7.8 and Denali fault Mw 7.9 strike-slip earthquakes with global P wave back projection imaging. Journal of Geophysical Research: Solid Earth, 114(B2).

Wang, D., & Mori, J. (2012). The 2010 Qinghai, China, earthquake: A moderate earthquake with supershear rupture. Bulletin of the Seismological Society of America, 102(1), 301-308.

Yue, H., Lay, T., Freymueller, J. T., Ding, K., Rivera, L., Ruppert, N. A., & Koper, K. D. (2013). Supershear rupture of the 5 January 2013 Craig, Alaska (Mw 7.5) earthquake. Journal of Geophysical Research: Solid Earth, 118(11), 5903-5919.

List of Tables

Table 1: 36 source models generated from combinations of uniform and heterogeneous rupture parameters using five different realizations (MOD-I, where I = 1, 2, 3, 4 and 5).			
Model Reference	D	Tr	Vr
U_{DTrVr}	U	U	U
MOD-I; H_D	H	U	U
MOD-I; H_{Tr}	U	H	U
MOD-I; H_{Vr}	U	U	H
MOD-I; H_{DTr}	H	H	U
MOD-I; H_{DVr}	H	U	H
MOD-I; H_{TrVr}	U	H	H
MOD-I	H	H	H

Table 2: Six 3D earth models generated from combinations of correlation lengths and standard deviations with fixed Hurst exponent.			
Model Reference	Correlation length a (km)	Standard deviation σ (%)	Hurst exponent H
M1	5.0	5	0.2
M2	2.0	5	0.2
M3	0.5	5	0.2
M4	5.0	10	0.2
M5	2.0	10	0.2
M6	0.5	10	0.2

List of Figures

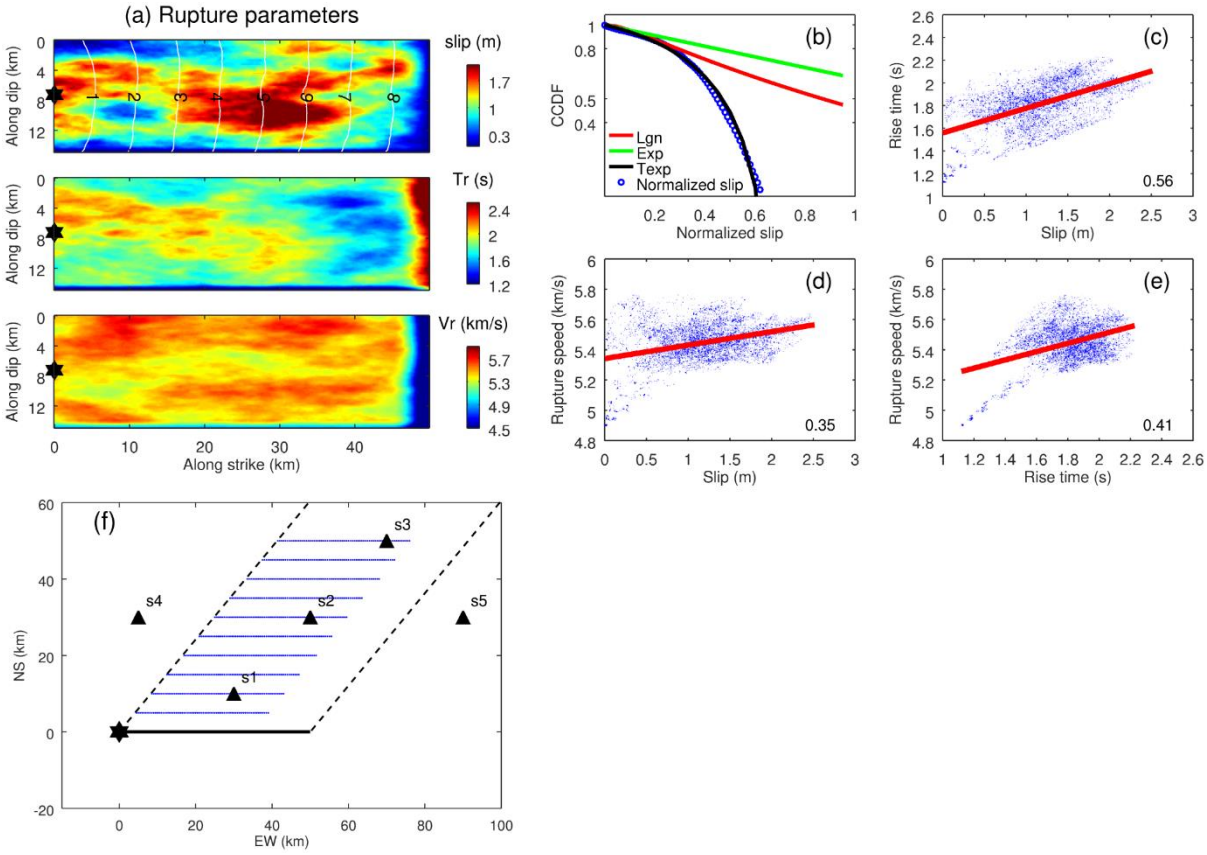

Figure 1: (a) Slip heterogeneities (white contours depict rupture time in seconds), rise time and supershear rupture speed variations (MOD-1) used for analyzing effects on Mach wave coherence. The black star marks the hypocenter. **(b)** Complementary cumulative distribution function (CCDF) of the slip compared against log-normal (Lgn), exponential (Exp) and truncated exponential (Texp) distributions. **(c), (d) and (e)** depicts correlations among rupture parameters (correlation coefficient is given in the bottom right of the plots and red line shows the linear least square fit). **(f)** Receiver geometry for ground-motion analysis (blue dots) as well as waveform comparison (black triangles, s1 to s5). The black dashed lines show the theoretically estimated Mach boundaries for rupture speed 1.57 Vs. The solid black line depicts the fault trace, the black star marks the epicenter.

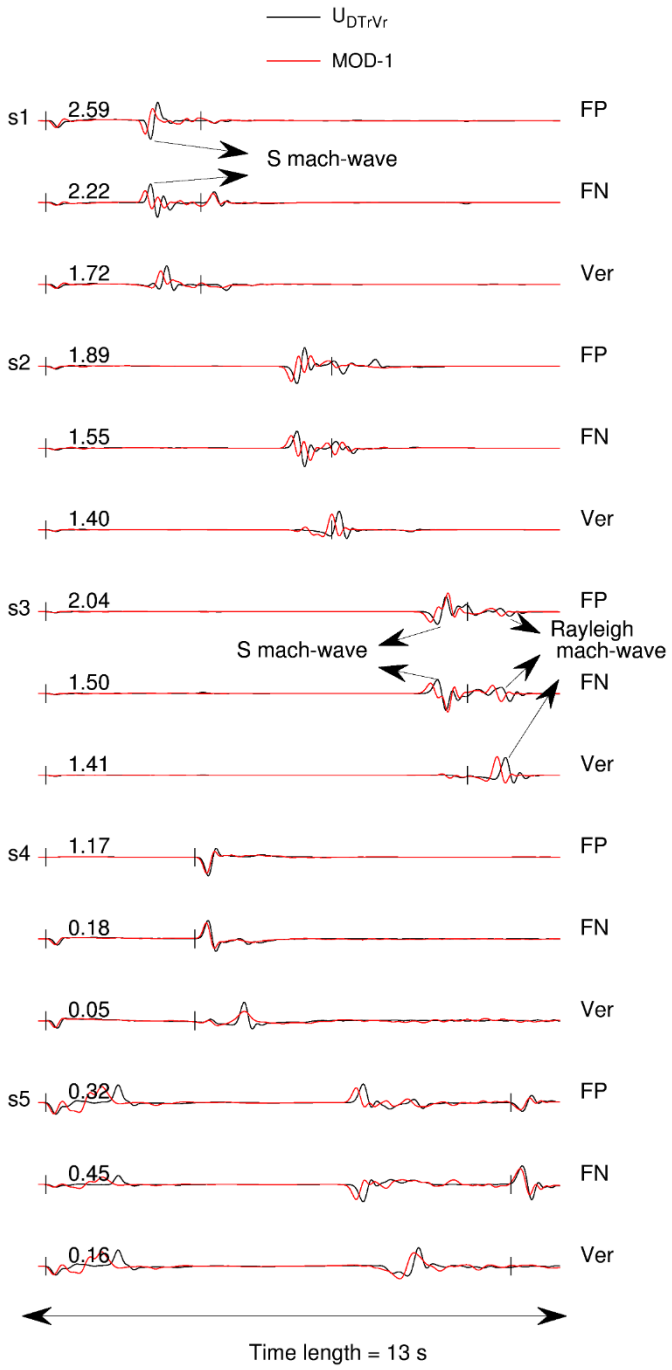

Figure 2: Ground acceleration (m/s^2) for fault-parallel (FP), fault-normal (FN), and vertical (Ver) components, comparing MOD-1 to the reference source U_{DTrVr} at five stations (s1 - s5, Figure 1-f). Theoretical arrivals from the epicenter of P- and S-waves (black bars) are also shown. Waveforms are aligned according to the theoretical P-wave arrival and normalized with respect to the absolute maximum of the two sources for a given component (indicated in upper left corner). The S-Mach-wave and Rayleigh-Mach-wave are also marked.

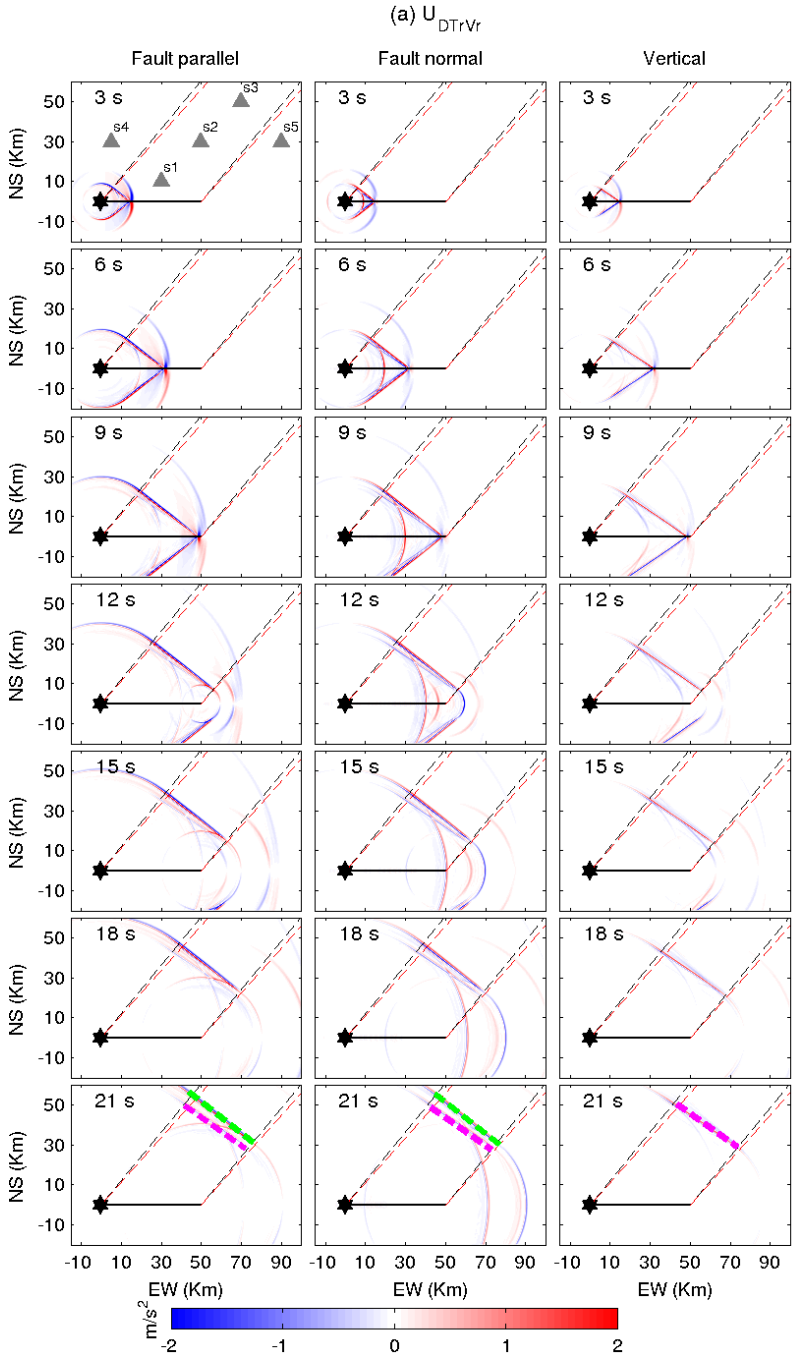
(a) U DTrVr
Fault parallel
Fault normal
Vertical
3 s
6 s
9 s
12 s
15 s
18 s
21 s
s1
s2
s3
s4
s5
NS (Km)
EW (Km)
50
30
10
-10
-10 10 30 50 70 90
m/s2
-2 -1 0 1 2

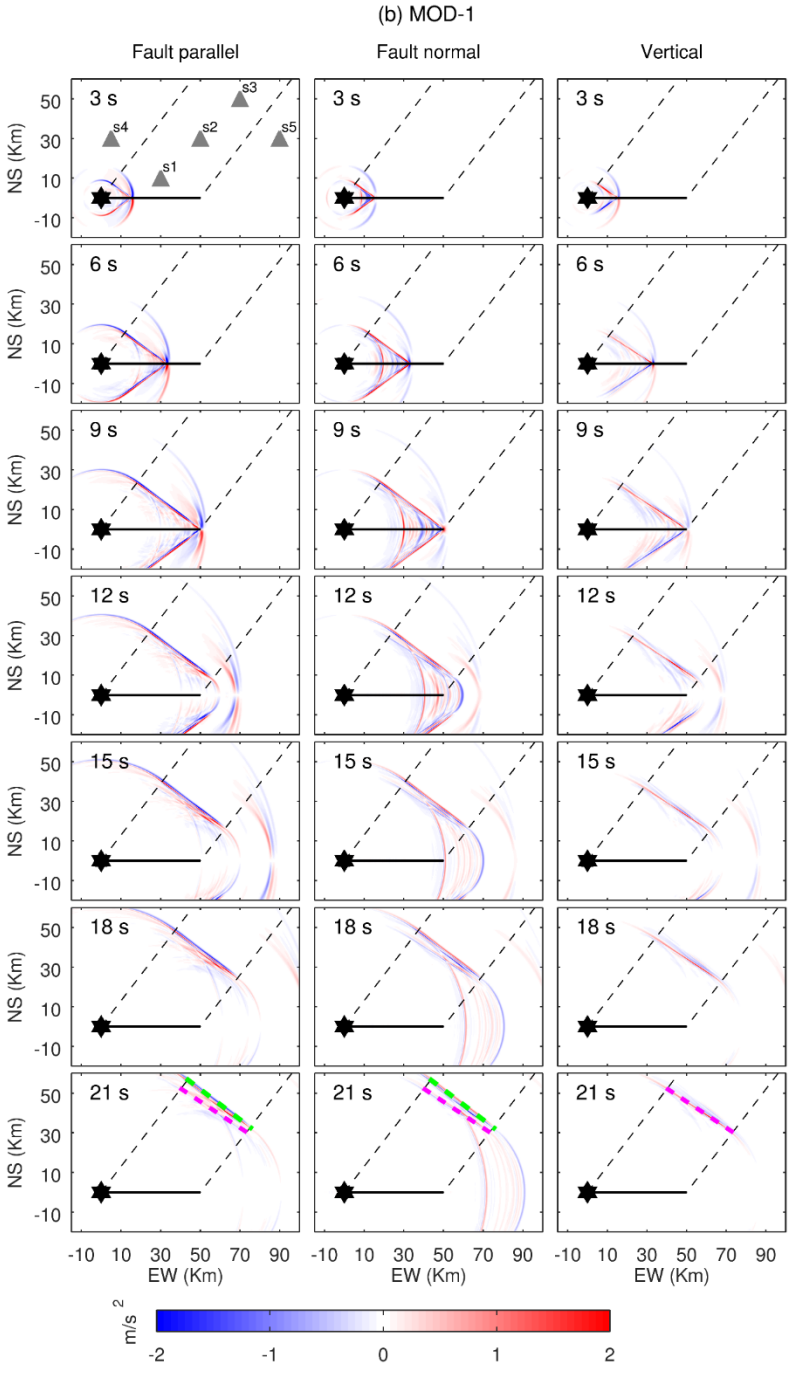

Figure 3: Snapshots of the ground-acceleration wavefield, for the three components of motion computed using the reference source U_{DTrVr} and MOD-1. The S-Mach-wave (green dashed line) and Rayleigh-Mach-wave (magenta dashed line) are marked to show their planar nature and orientation with respect to the fault. The Mach waves travel large distances from the fault without any attenuation.

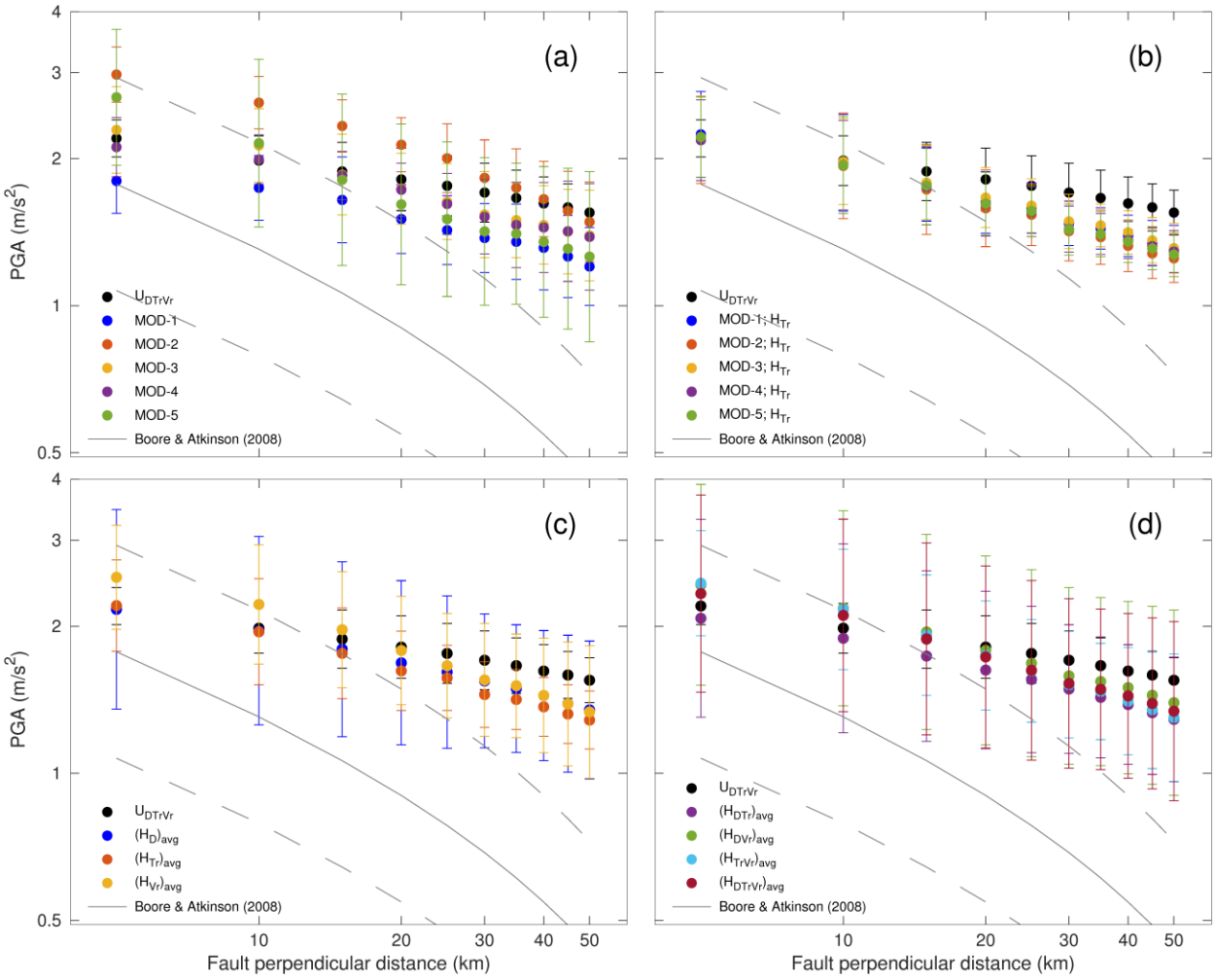

Figure 4: (a, b) PGA as a function of distance for eleven rupture models depicts the effects of rupture heterogeneity on ground motions generated from supershear ruptures. The mean (circles) and standard deviation (bars) of PGA are computed using stations at a given fault-perpendicular distance. The median (solid line) and 1-sigma bounds (dashed lines) of PGA from BA2008 are shown for comparison. Notice the variations of mean PGA for sources having heterogeneities in D, Tr and Vr (left top plot) with respect to U_{DTrVr}. The rupture models having heterogeneities only in rise time (right top plot) lead to equal/lower mean PGA compared to reference source. **(c, d)** PGA averaged over five realizations for a given heterogeneity (So, five PGA curves in Fig. 4-a corresponding to MOD-1, 2, 3, 4, 5 is represented by one curve in Fig. 4-d as $(H_{DTrVr})_{avg}$) as function of distance showing overall effects of rupture parameters heterogeneities on mach-wave coherence.

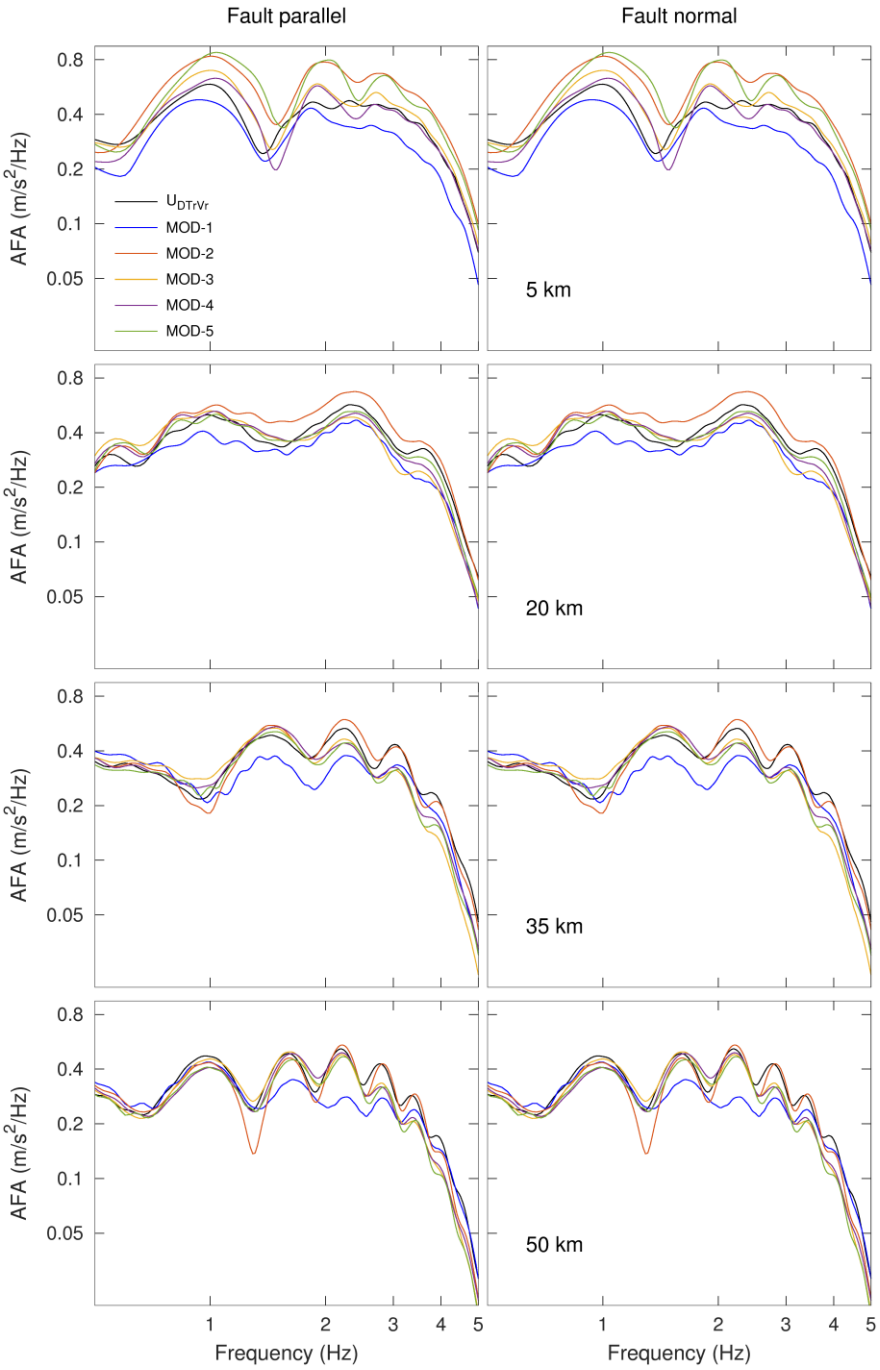

Figure 5: Average Fourier amplitude (AFA) spectra as a function of frequency for the fault-parallel (FP) and fault-normal (FN) components of ground motion for six source models at different fault perpendicular distances (5, 20 35, 50 km). Notice the variations of AFA for different rupture models compared to reference source.

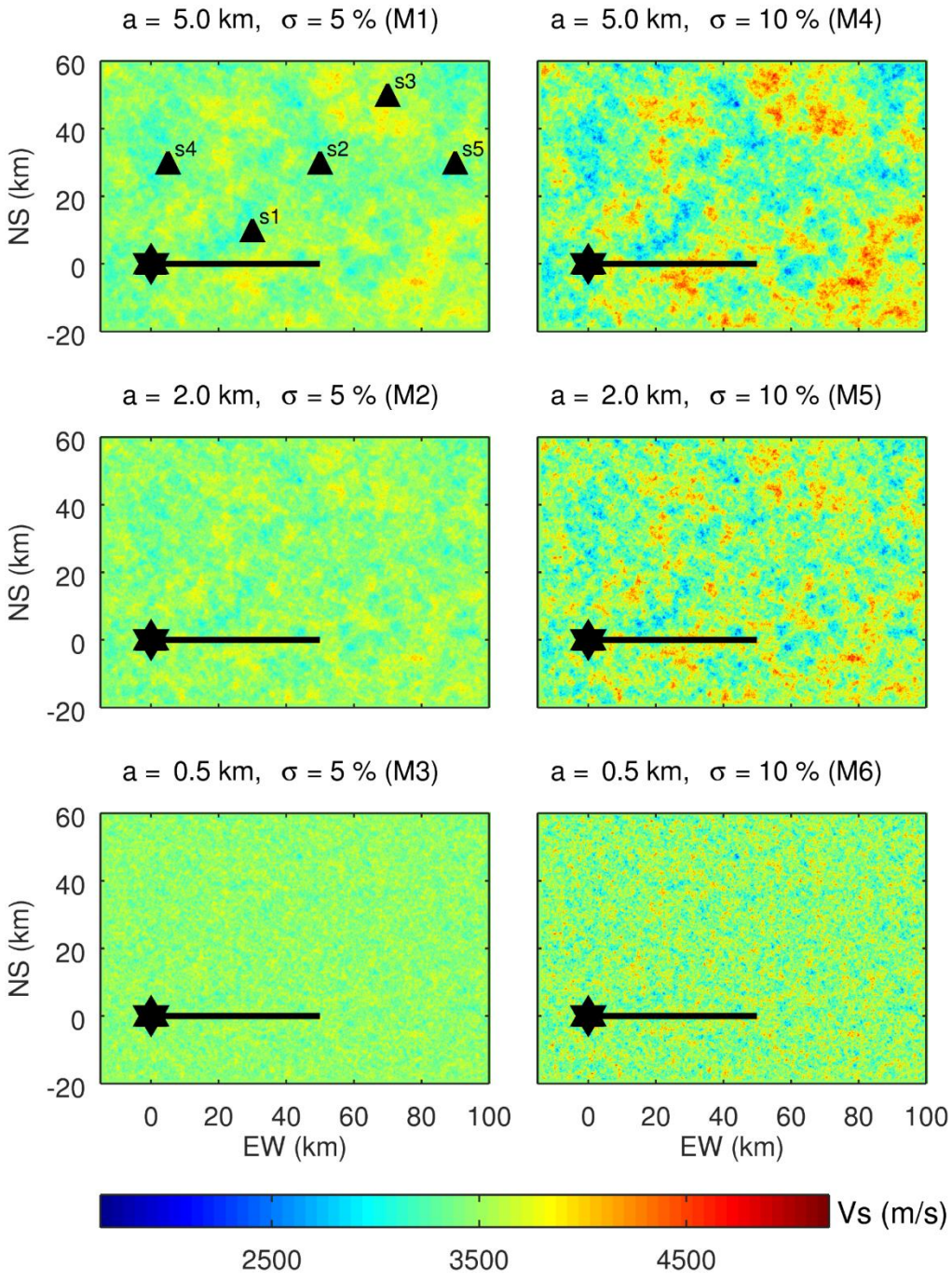

Figure 6: Surface slices of shear-wave speed for the six realizations of 3D random Earth models, using combinations of three correlation lengths (5.0 km, 2.0 km, 0.5 km) and two standard deviations (5%, 10%) for fixed Hurst exponent (H = 0.2). The solid black line depicts the fault trace; the black star marks the epicenter.

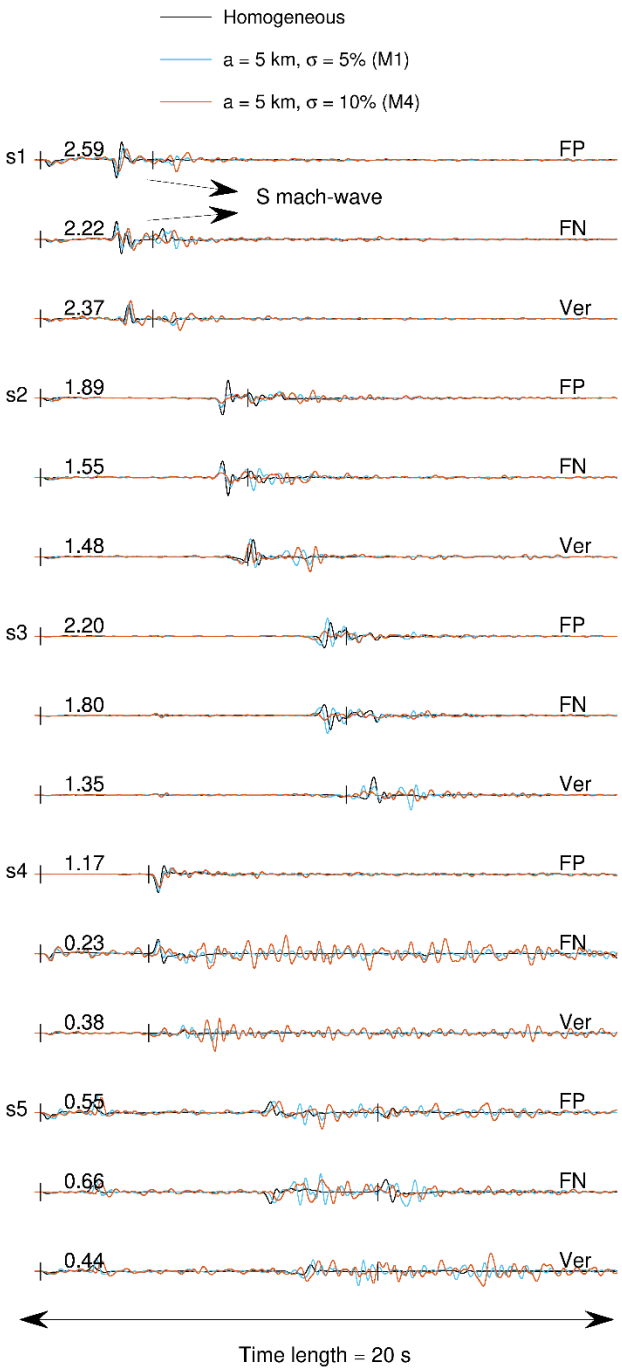

Figure 7: Ground acceleration (m/s^2) for the fault-parallel (FP), fault-normal (FN) and Vertical (Ver) components, comparing two heterogeneous media M1 and M4 with the homogeneous medium at five stations (s1 - s5, Figure 1-f). Theoretical P- and S-wave arrival times (for the homogeneous medium) are shown for reference. Waveforms are aligned according to the theoretical P-wave arrival time, and are normalized with respect to absolute maximum of motion within the three media for a given component (indicated in upper left corner).

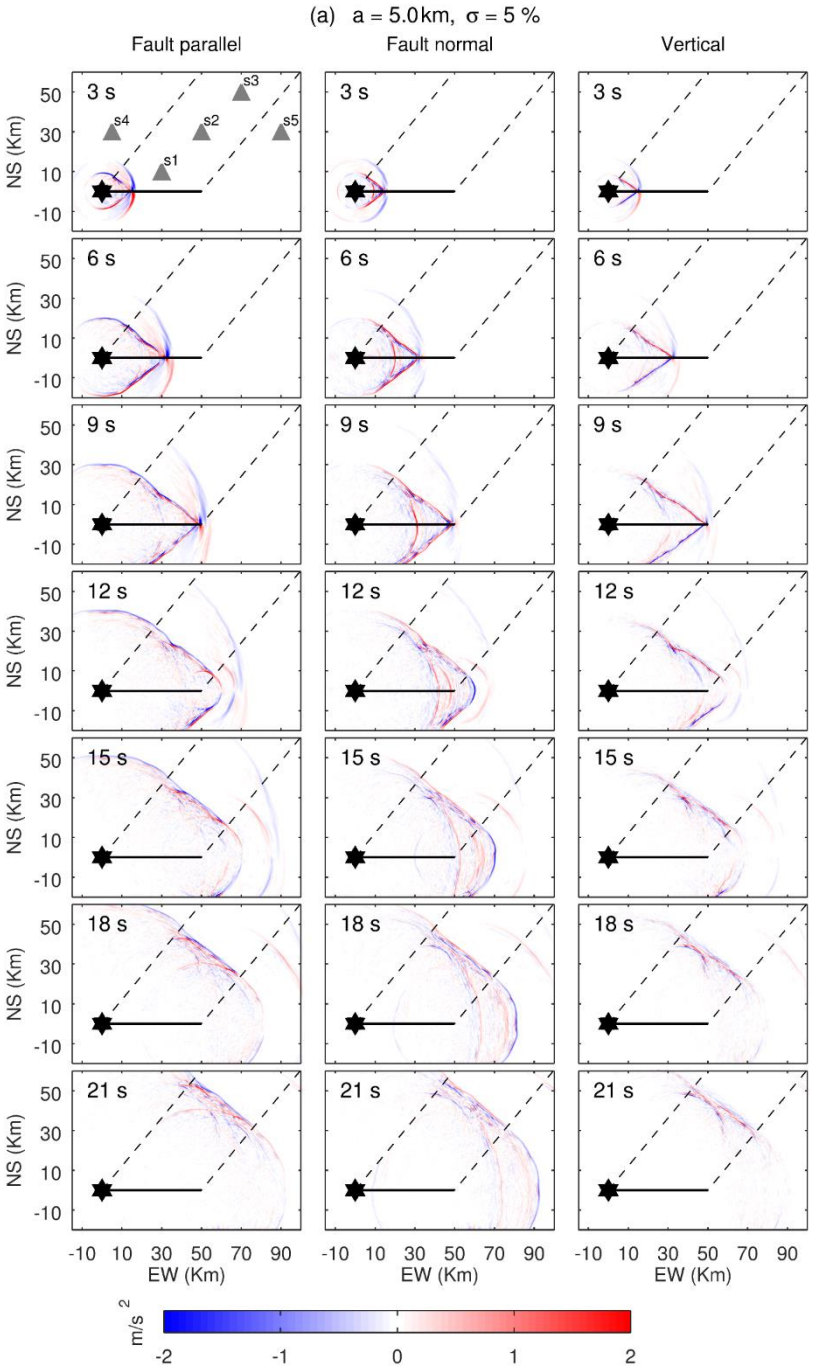
(a) a = 5.0km, σ = 5 %
Fault parallel
Fault normal
Vertical
3 s
6 s
9 s
12 s
15 s
18 s
21 s
s1
s2
s3
s4
s5
NS (Km)
EW (Km)
50
30
10
-10
-10 10 30 50 70 90
m/s2
-2
-1
0
1
2

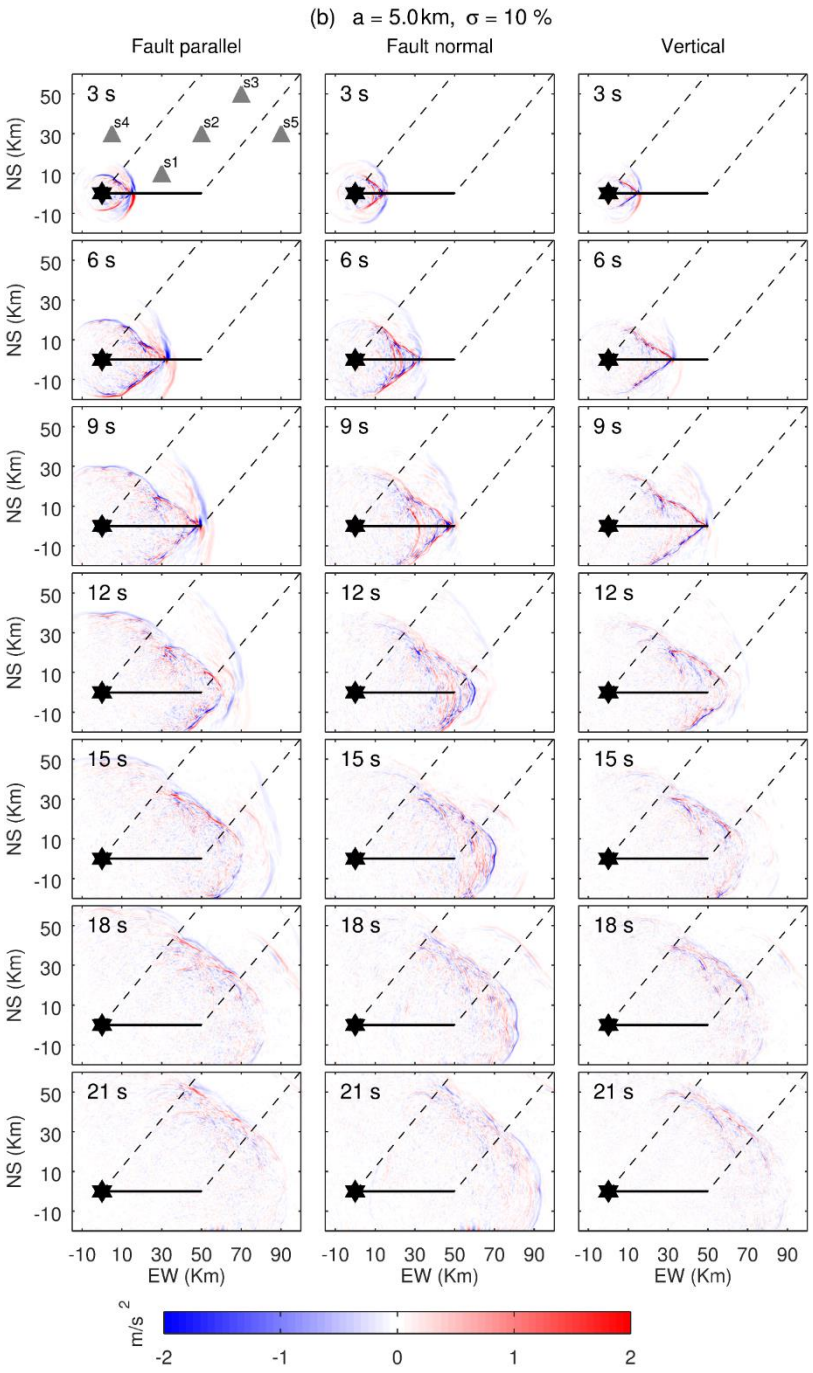

Figure 8: Snapshots in time of the acceleration wavefield at the Earth-surface for three components (FP, FN, and Ver) for media M1 (a = 5.0 km, σ = 5%) and M4 (a = 5.0 km, σ = 10%). As the Mach wave travels away from the fault, peak amplitudes decrease due to seismic scattering. Scattering effects, and hence amplitude reductions, are larger for medium with σ = 10%.

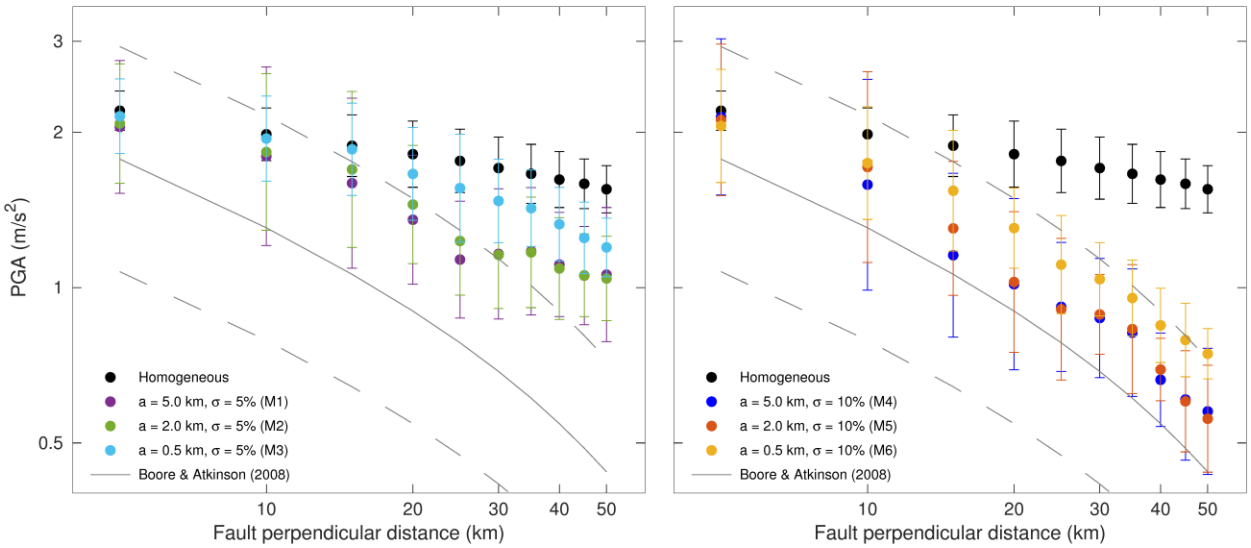

Figure 9: PGA as function of distance for six heterogeneous media and the homogeneous medium depicts the effects of seismic scattering on ground-shaking levels from supershear ruptures. The mean (circles) and standard deviation (bars) of PGA are computed using stations at given fault perpendicular distance; median (solid line) and 1-sigma bounds (dashed lines) of PGA-estimates from BA2008 are plotted for comparison. Notice how small-scale media heterogeneities lower the mean PGA, especially for M4 and M5 (blue and orange dots).

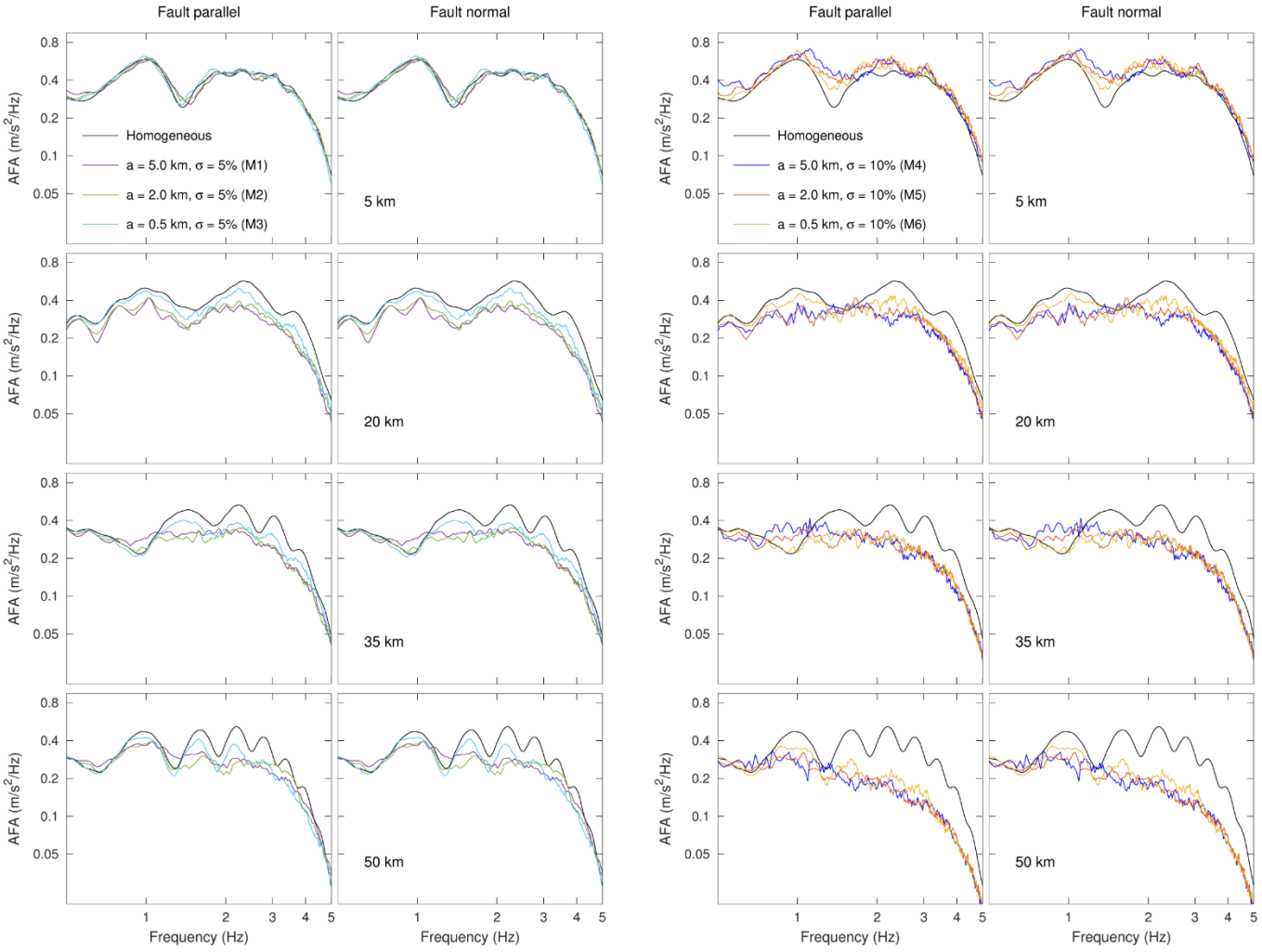

Figure 10: Average Fourier amplitudes (AFA) as a function of frequency for fault-parallel (FP) and fault-normal (FN) components of ground motion for the six heterogeneous media and homogeneous medium at different fault perpendicular distances (5, 20 35, 50 km). The AFA decreases with increasing distance from the fault. But we note that, the AFA decline with distance for M4, M5 and M6 is considerably larger for than M1, M2 and M3.

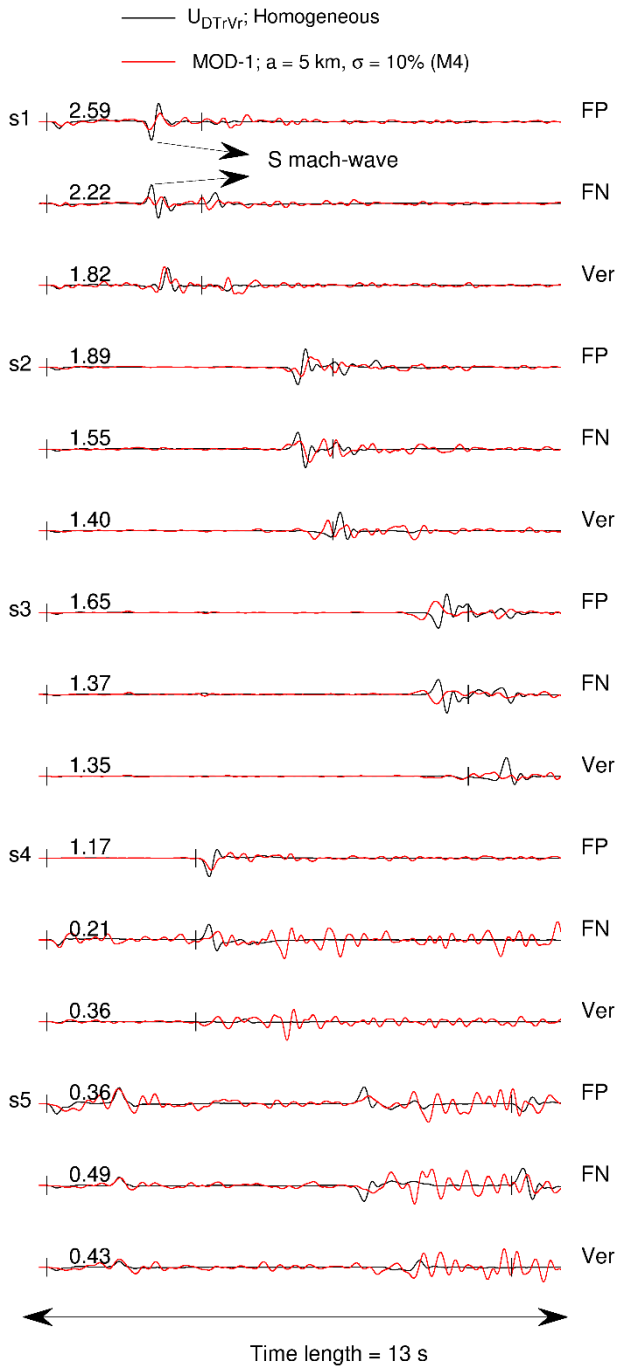

Figure 11: Ground acceleration (m/s^2) for the fault-parallel (FP), fault-normal (FN) and Vertical (Ver) components, comparing MOD-1 in M4 to U_{DTrVr} in the homogeneous medium at five stations (s1 - s5, Figure 1-f). The theoretical P- and S-wave arrival times in the homogeneous medium are shown for reference. Waveforms are aligned according to the epicentral P-arrival time and normalized with respect to absolute maximum of two signals for a given component (indicated in the upper left corner).

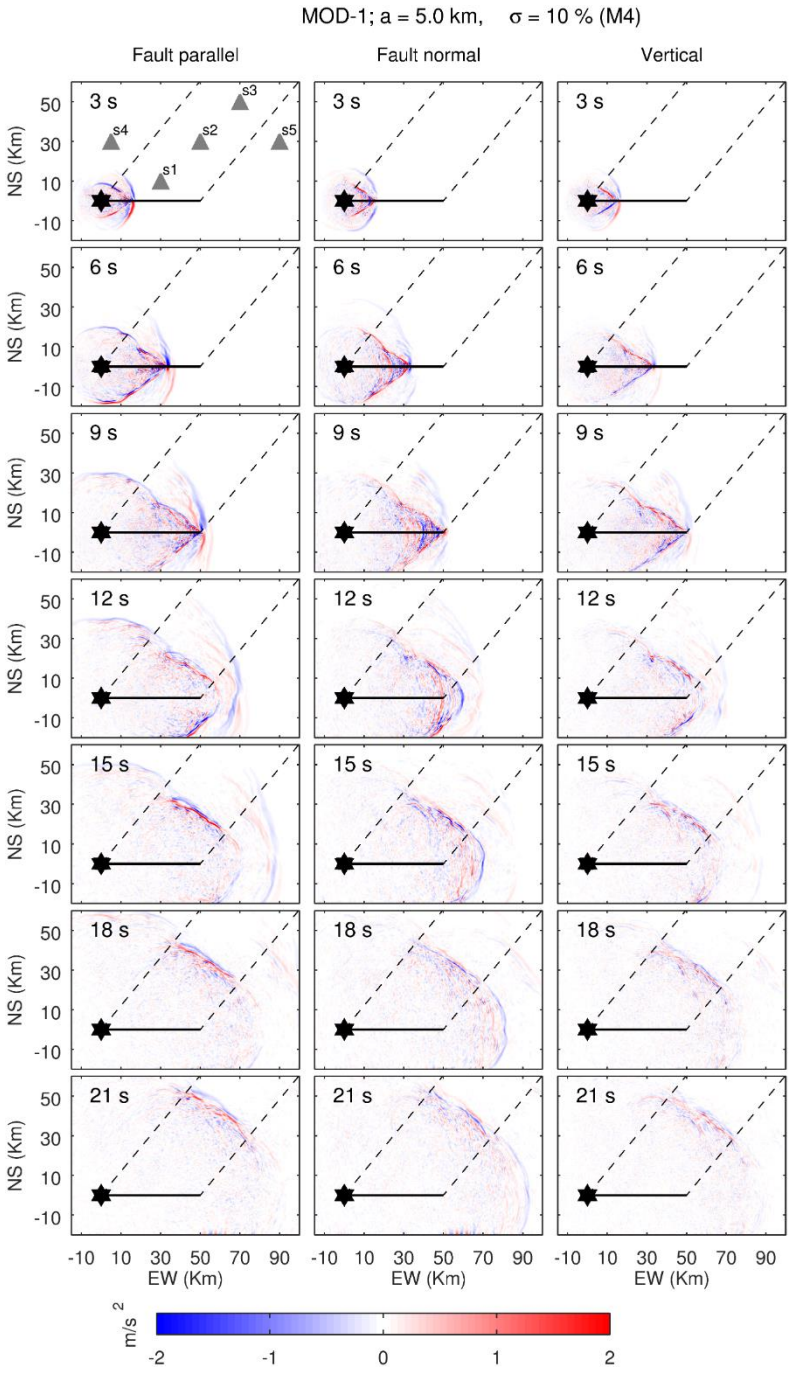

Figure 12: Snapshots in time of the acceleration wavefield at the Earth-surface for the three components for source model MOD-1 in M4. Rupture parameters heterogeneities of MOD-1 lower the Mach wave amplitudes, which are then further reduced by scattering as the Mach wave travels away from the fault.

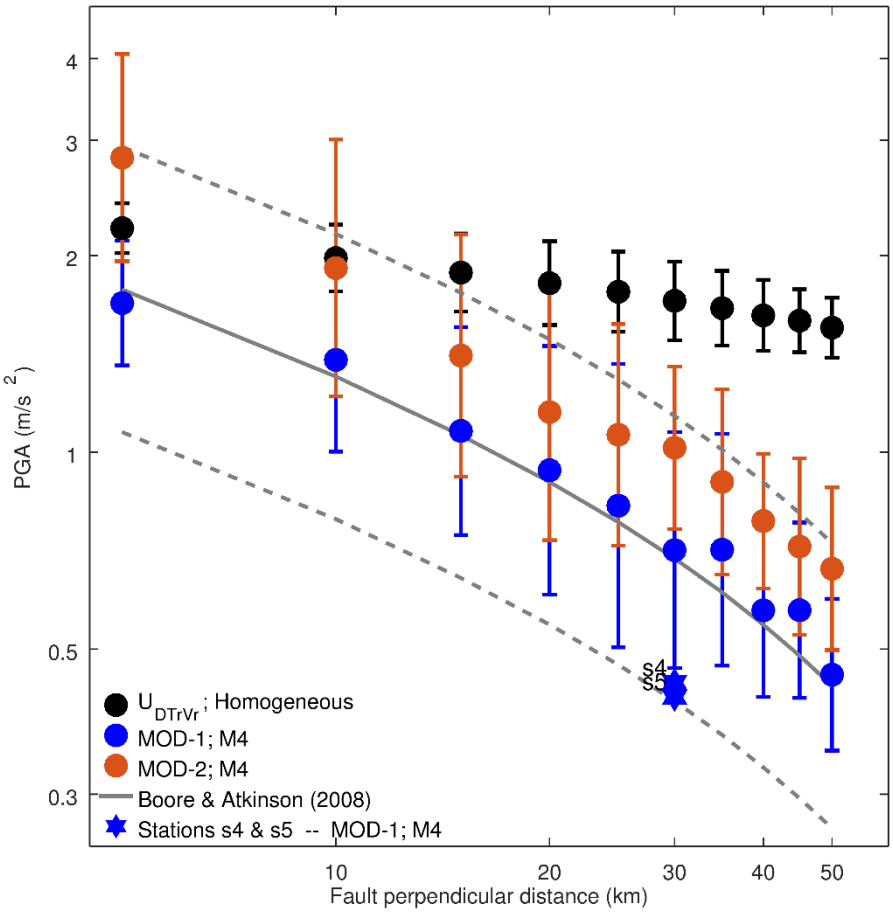

Figure 13: PGA as a function of distance for sources MOD–1, 2 in M4, and U_{DTrVr} in the homogeneous medium. The comparisons show the effects of combined source and medium heterogeneities on ground-motion levels. The median (solid line) and 1-sigma bounds (dashed lines) of PGA–estimates from BA2008 are also plotted for reference. Notice that PGA values for MOD–1,2 in M4 are comparable to BA2008 (MOD-1 being closer to BA2008), and that PGA at stations s4 and s5 (outside theoretical Mach cone boundary) are within the one-sigma bounds of BA2008.

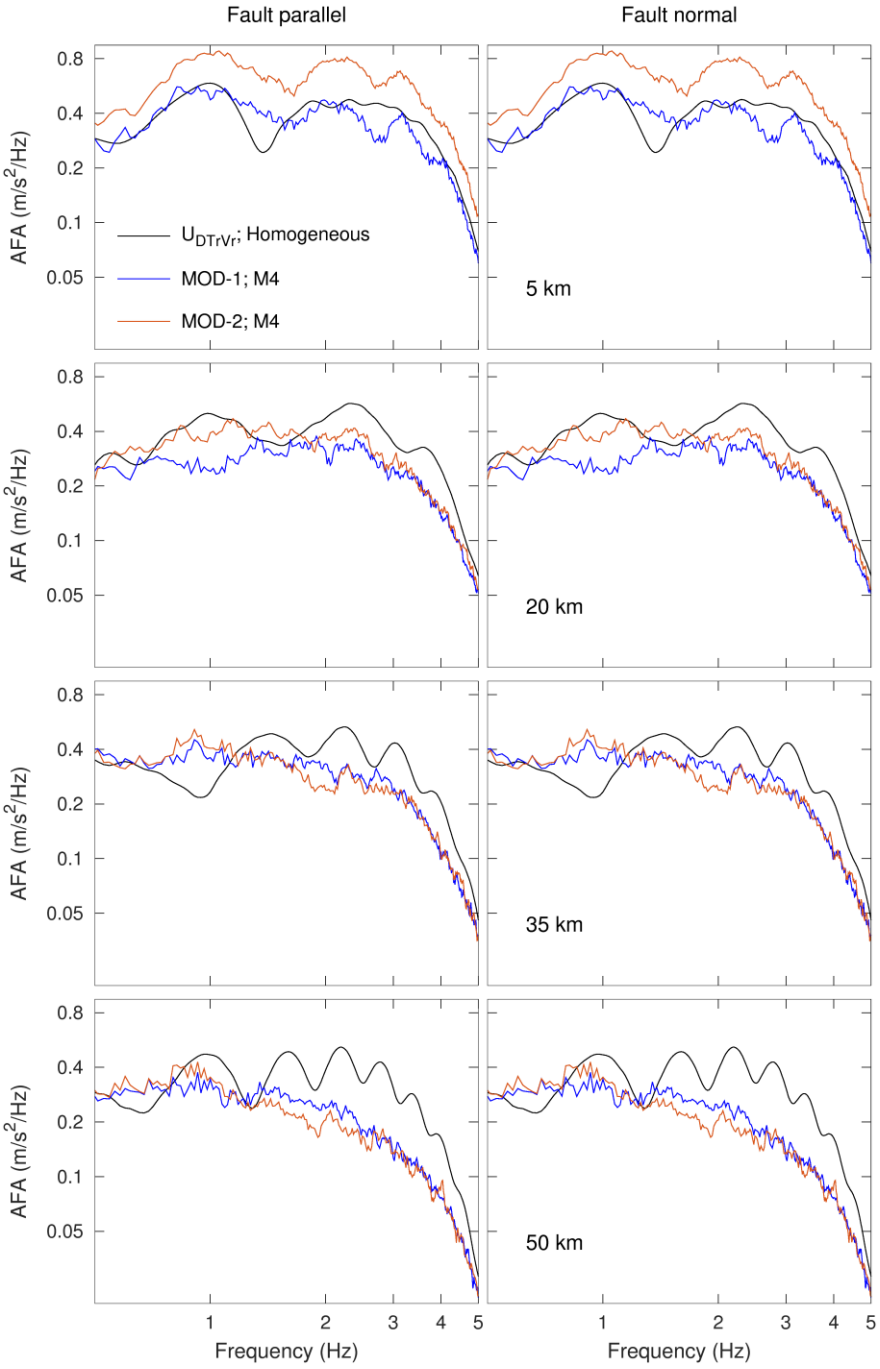

Figure 14: Average Fourier amplitudes (AFA) as a function of frequency for the two horizontal components of ground motions for source models MOD–1, 2 in medium M4, and source U_{DTrVr} in the homogeneous medium. The AFA decreases with increasing distance from the fault for MOD–1,2 in M4 for frequencies above 1 Hz.

Electronic Supplement

Mach wave properties in the presence of source and medium heterogeneity

J. C. Vyas[1], P. M. Mai[1], M. Galis[1,4], Eric M. Dunham[2], and W. Imperatori[3]

[1]King Abdullah University of Science and Technology, [2]Stanford University, [3]Swiss Seismological Service, ETH Zurich, [4]Comenius University, Bratislava.

Email: Jagdish.Vyas@kaust.edu.sa

The electronic supplement contains several source models showing rupture parameters distributions, correlations among them and one point statistics of slip. Additionally, it contains ground velocity waveforms and snapshots at Earth surface depicting the effects of rupture complexity and wavefield scattering for supershear ruptures. The peak ground acceleration (PGA) statistics and average Fourier acceleration (AFA) are computed to further quantify source heterogeneity effects (Figure 1 shows the receiver geometry).

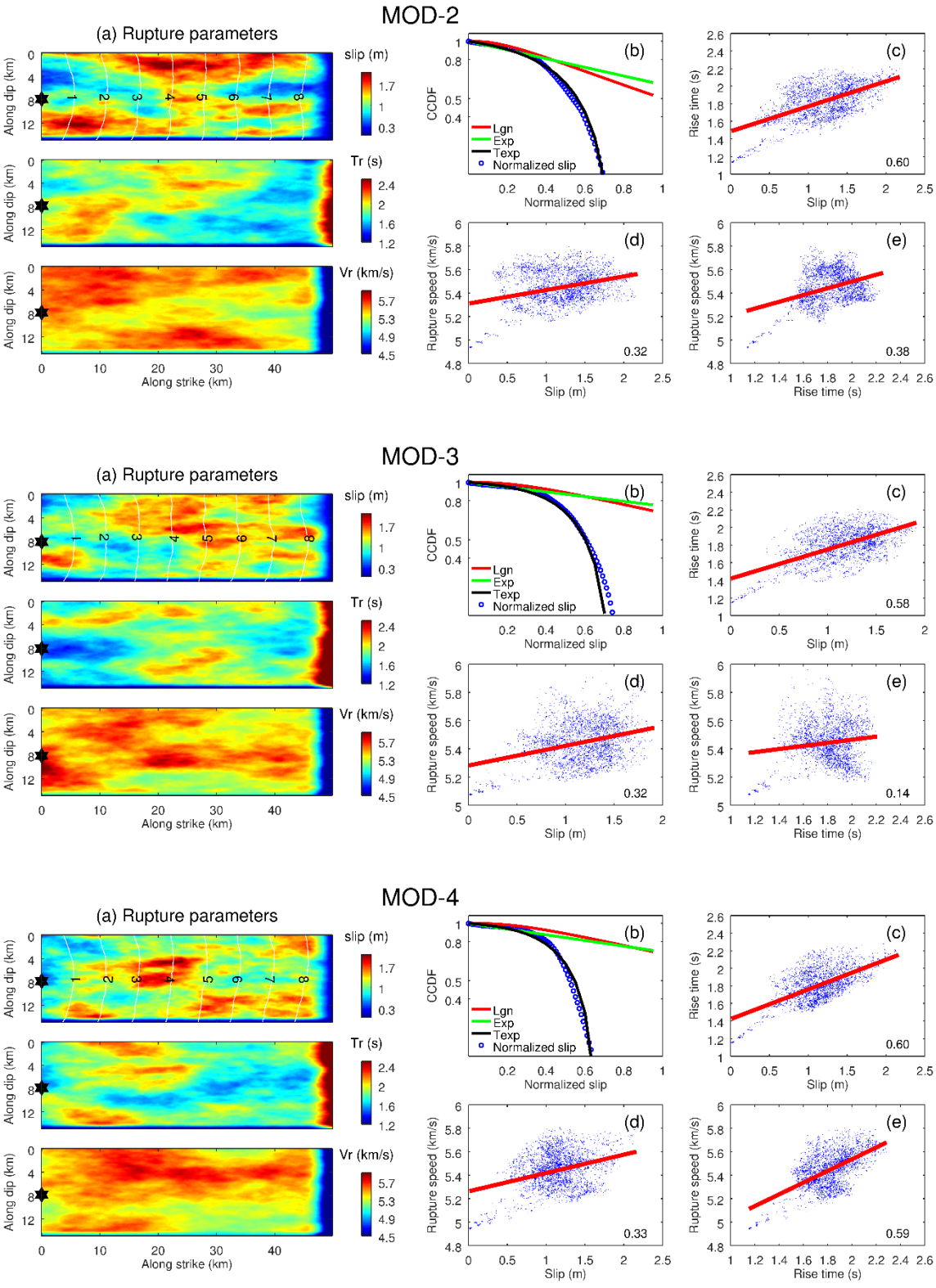
MOD-2
(a) Rupture parameters
slip (m)
Tr (s)
Vr (km/s)
Along dip (km)
Along strike (km)
(b)
CCDF
Lgn
Exp
Texp
Normalized slip
(c)
Rise time (s)
Slip (m)
0.60
(d)
Rupture speed (km/s)
0.32
(e)
0.38
MOD-3
(a) Rupture parameters
(b)
(c)
0.58
(d)
0.32
(e)
0.14
MOD-4
(a) Rupture parameters
(b)
(c)
0.60
(d)
0.33
(e)
0.59

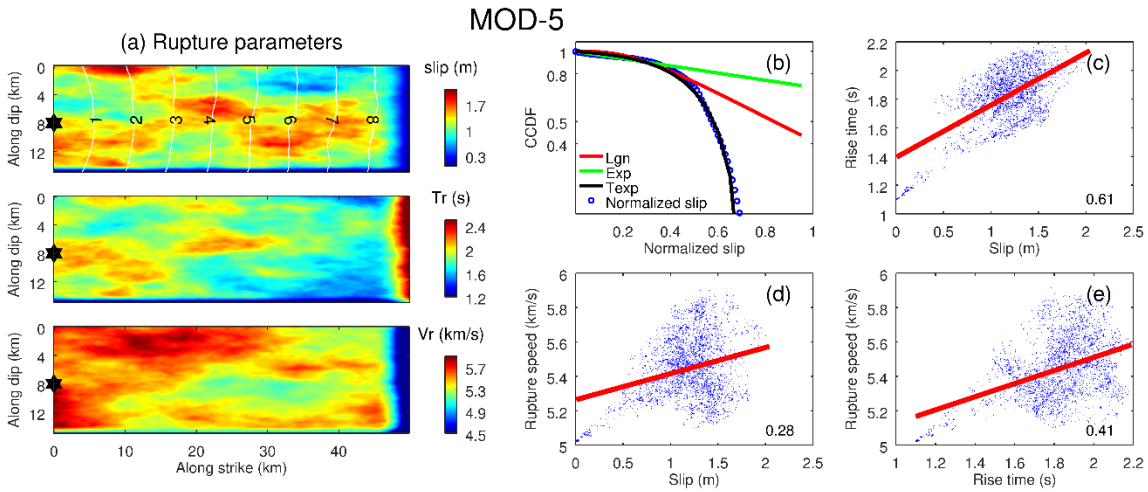

Figure S1: (a) Slip heterogeneities (white contours depict rupture time in seconds), rise time and supershear rupture speed variations (MOD-2, MOD-3, MOD-4, MOD-5) used for analyzing effects on Mach wave coherence. The black star marks the hypocenter. **(b)** Complementary cumulative distribution function (CCDF) of the slip compared against log-normal (Lgn), exponential (Exp) and truncated exponential (Texp) distributions. **(c), (d) and (e)** depicts correlations among rupture parameters (correlation coefficient is given in the bottom right of the plots and the red line shows linear least square fit).

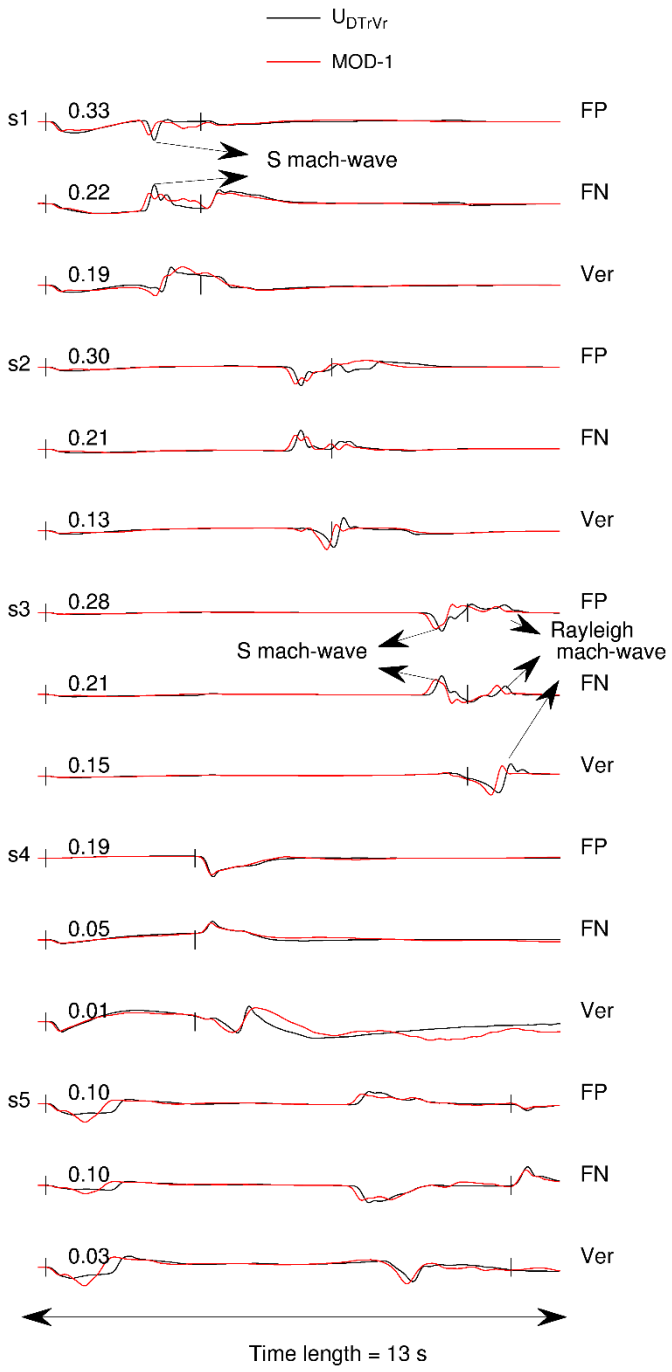

Figure S2: Ground velocity (m/s) for fault parallel (FP), fault normal (FN), and vertical (Ver) components, comparing MOD-1 to the reference source U_{DTrVr} at five stations (s1 - s5, Figure 1-f). Theoretical arrivals from the epicenter of P- and S-waves (black bars) are also shown. Waveforms are aligned according to the theoretical P-wave arrival and normalized with respect to the absolute maximum of the two sources for a given component (indicated in upper left corner). The S-Mach-wave and Rayleigh-Mach-wave are also marked.

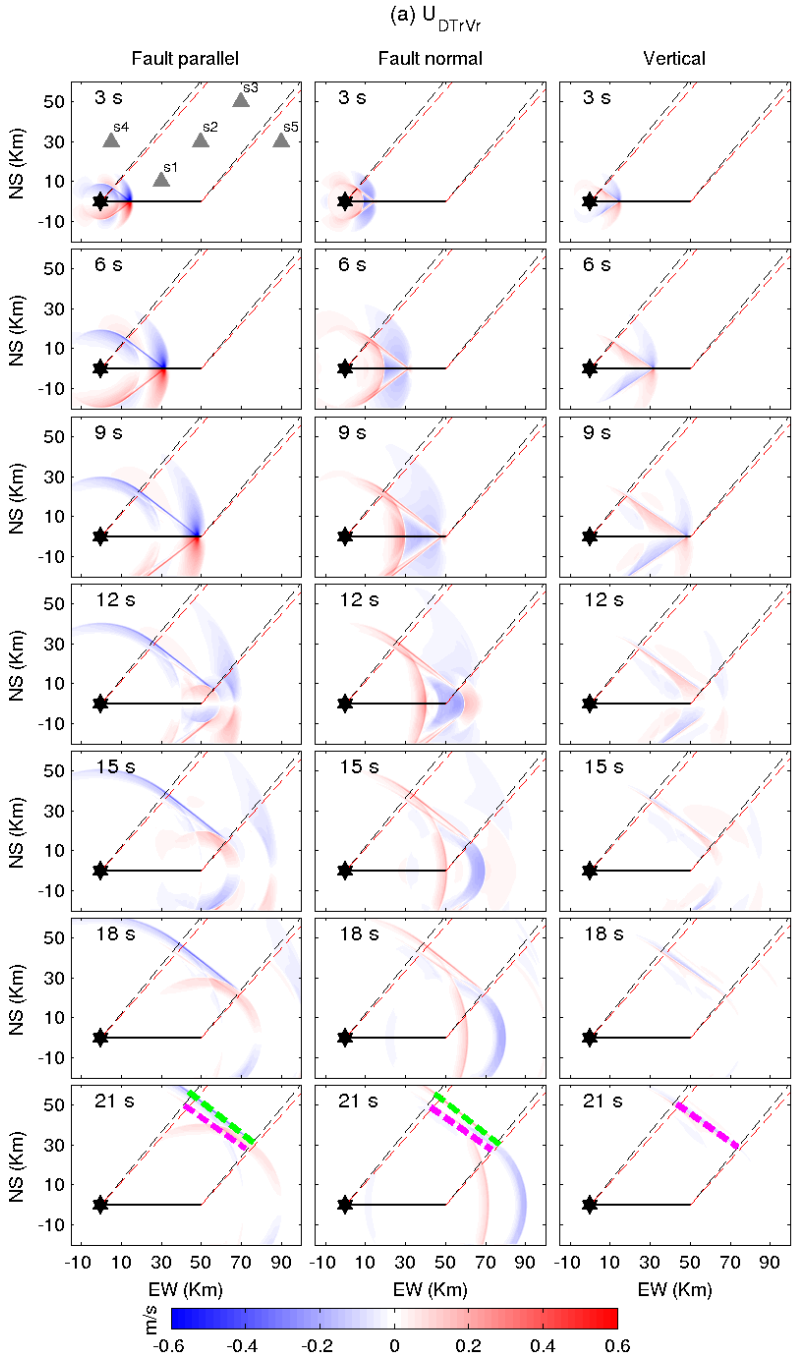
(a) U DTrVr
Fault parallel
Fault normal
Vertical
3 s
6 s
9 s
12 s
15 s
18 s
21 s
s1
s2
s3
s4
s5
NS (Km)
EW (Km)
m/s
-0.6
-0.4
-0.2
0
0.2
0.4
0.6

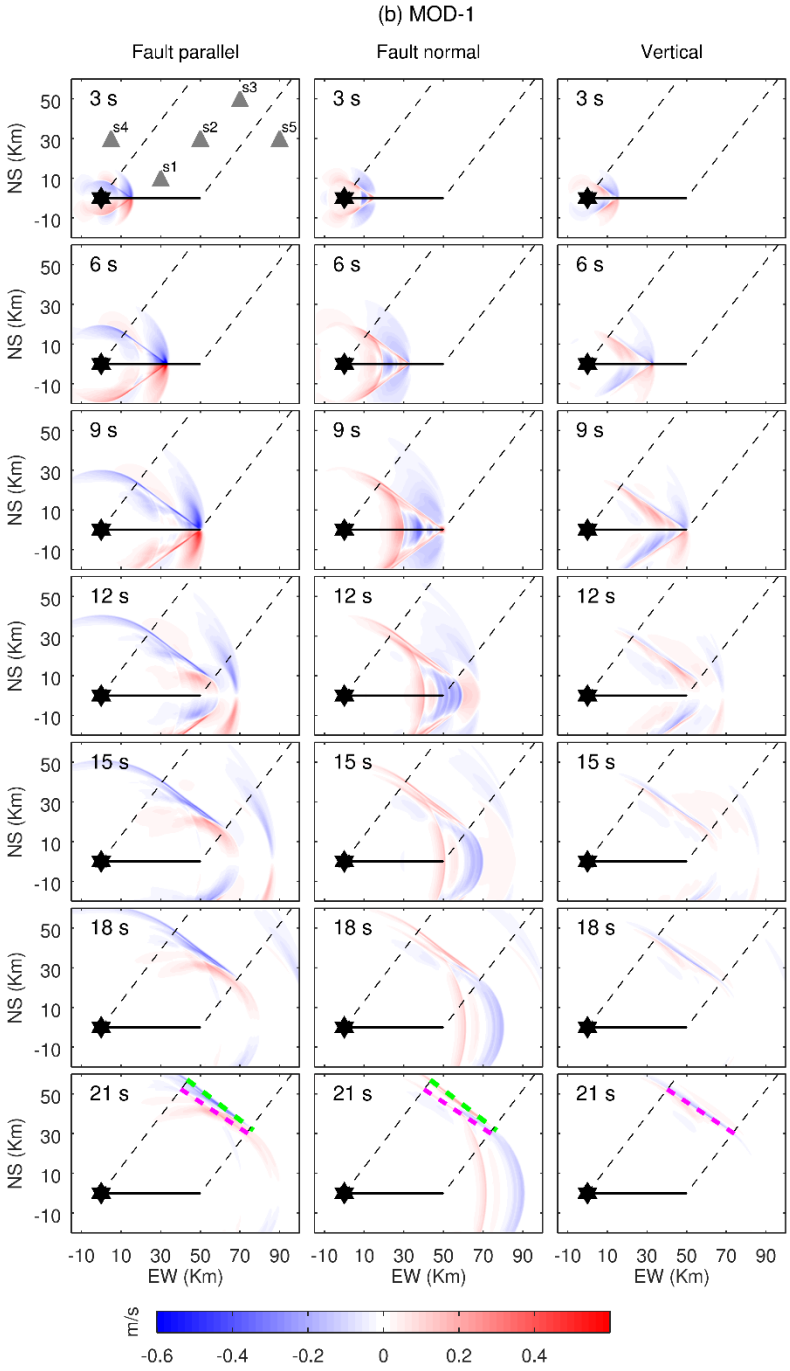

Figure S3: Snapshots of the ground-velocity wavefield, for three components of motion computed using the reference source U_{DTrVr} and MOD-1. The S-Mach-wave (green dashed line) and Rayleigh-Mach-wave (magenta dashed line) are marked to show their planar nature and orientation with respect to the fault. The Mach waves travel large distances from the fault without any attenuation.

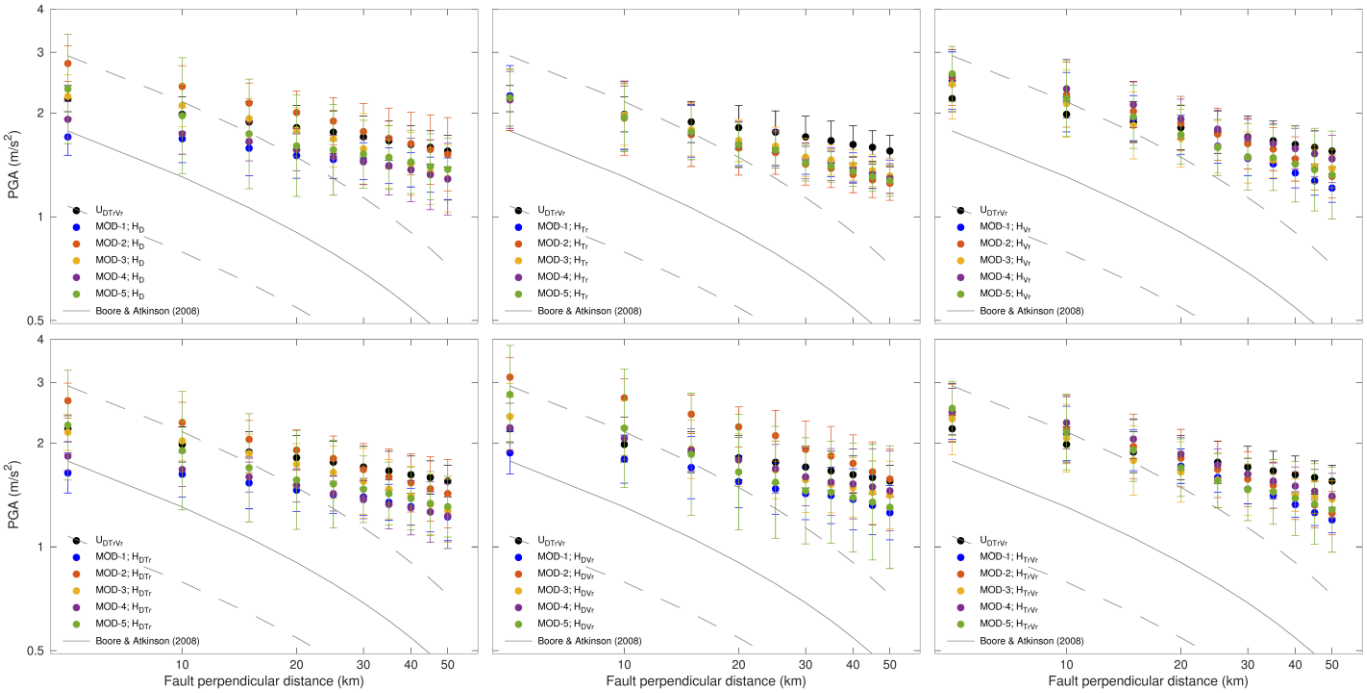

Figure S4: PGA as a function of distance for thirty-one rupture models depicts the effects of rupture heterogeneity on ground motions generated from supershear ruptures. The mean (circles) and standard deviation (bars) of PGA are computed using stations at a given fault-perpendicular distance. The median (solid line) and 1-sigma bounds (dashed lines) of PGA from BA2008 are shown for comparison. Notice a clear trend for rupture models having heterogeneities only in rise time leading to equal/lower mean PGA compared to reference source.

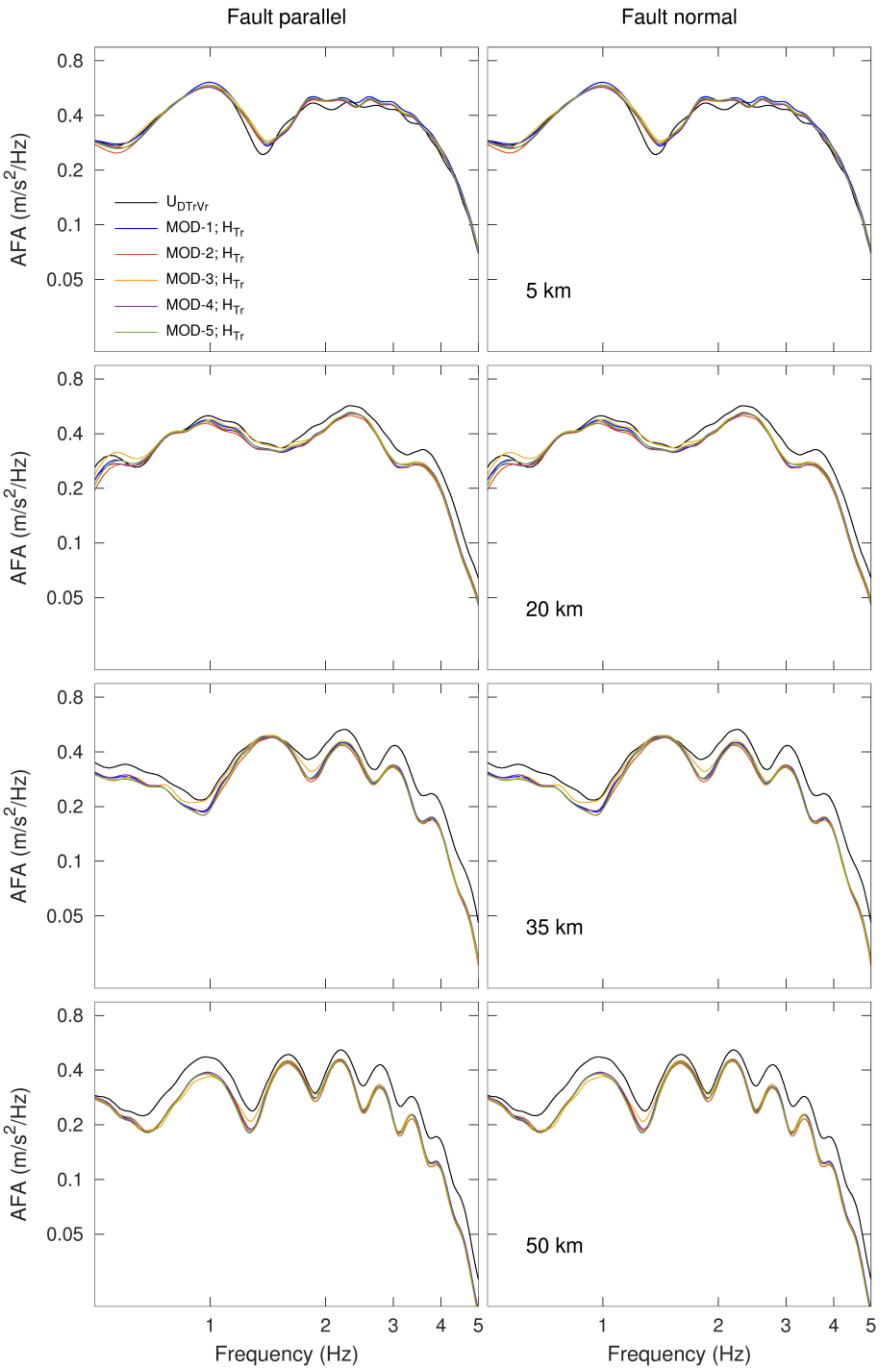

Figure S5: Average Fourier amplitude (AFA) spectra as a function of frequency for the fault-parallel (FP) and fault-normal (FN) components of ground motion for six source models at different fault perpendicular distances (5, 20 35, 50 km). The AFA for rupture models having heterogeneities only in rise time is comparable or lower than reference source.

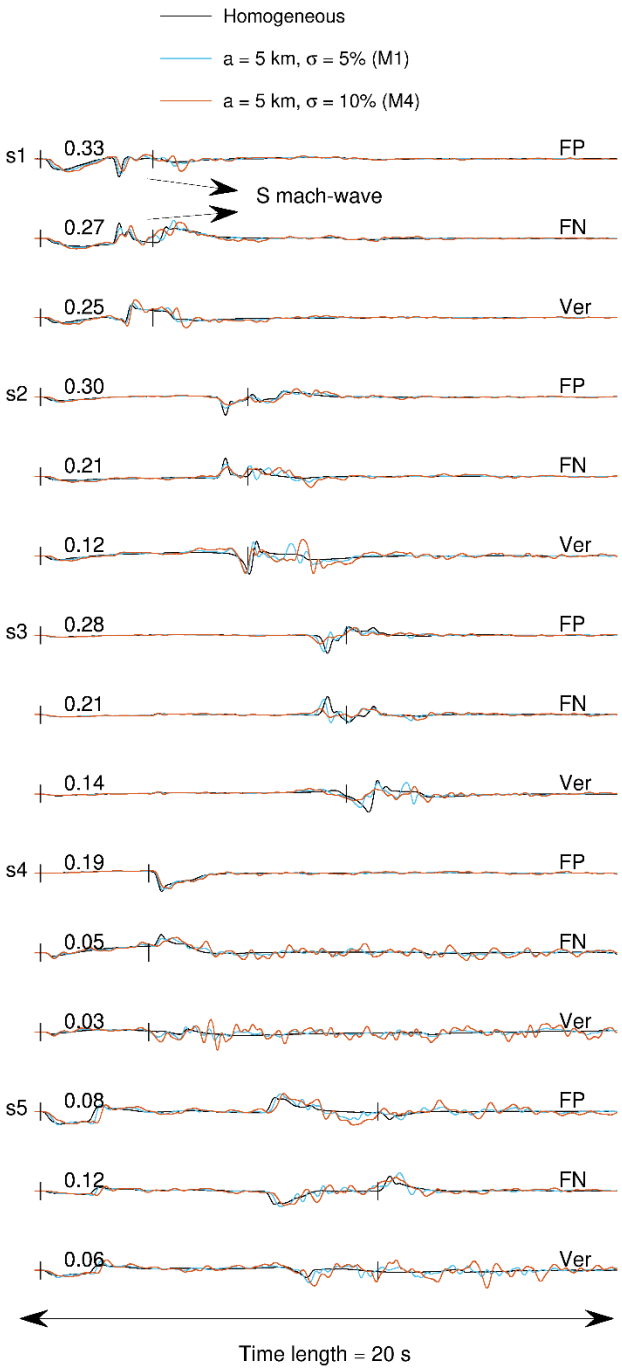

Figure S6: Ground velocity (m/s) for the fault-parallel (FP), fault-normal (FN) and Vertical (Ver) components, comparing two heterogeneous media M1 and M4 with the homogeneous medium at five stations (s1 - s5, Figure 1-f). Theoretical P- and S-wave arrival times (for the homogeneous medium) are shown for reference. Waveforms are aligned according to the epicentral P-wave arrival time and normalized with respect to the absolute maximum of motion within the three media for a given component (indicated in the upper left corner).

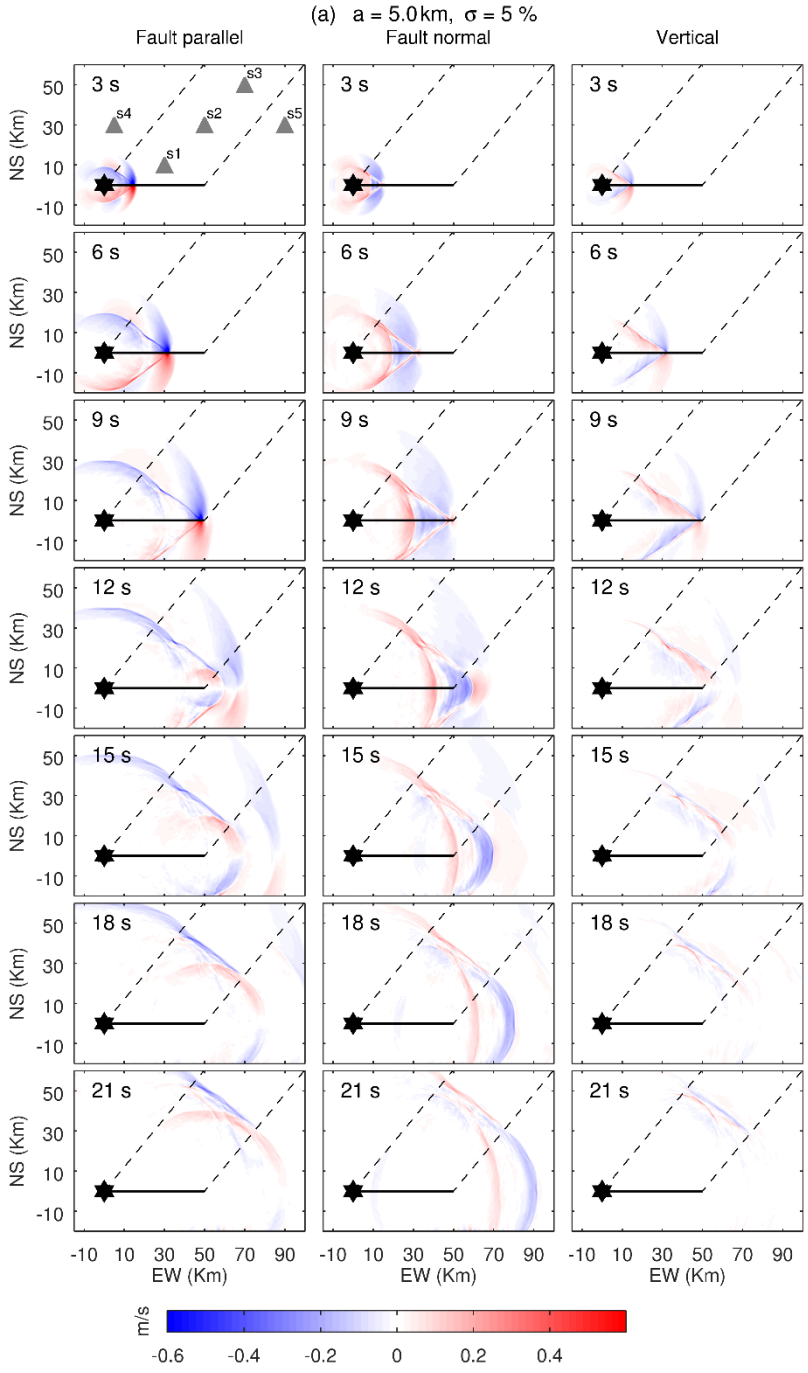
(a) a = 5.0 km, σ = 5 %
Fault parallel
Fault normal
Vertical
3 s
6 s
9 s
12 s
15 s
18 s
21 s
s1
s2
s3
s4
s5
NS (Km)
EW (Km)
50
30
10
-10
-10 10 30 50 70 90
m/s
-0.6 -0.4 -0.2 0 0.2 0.4

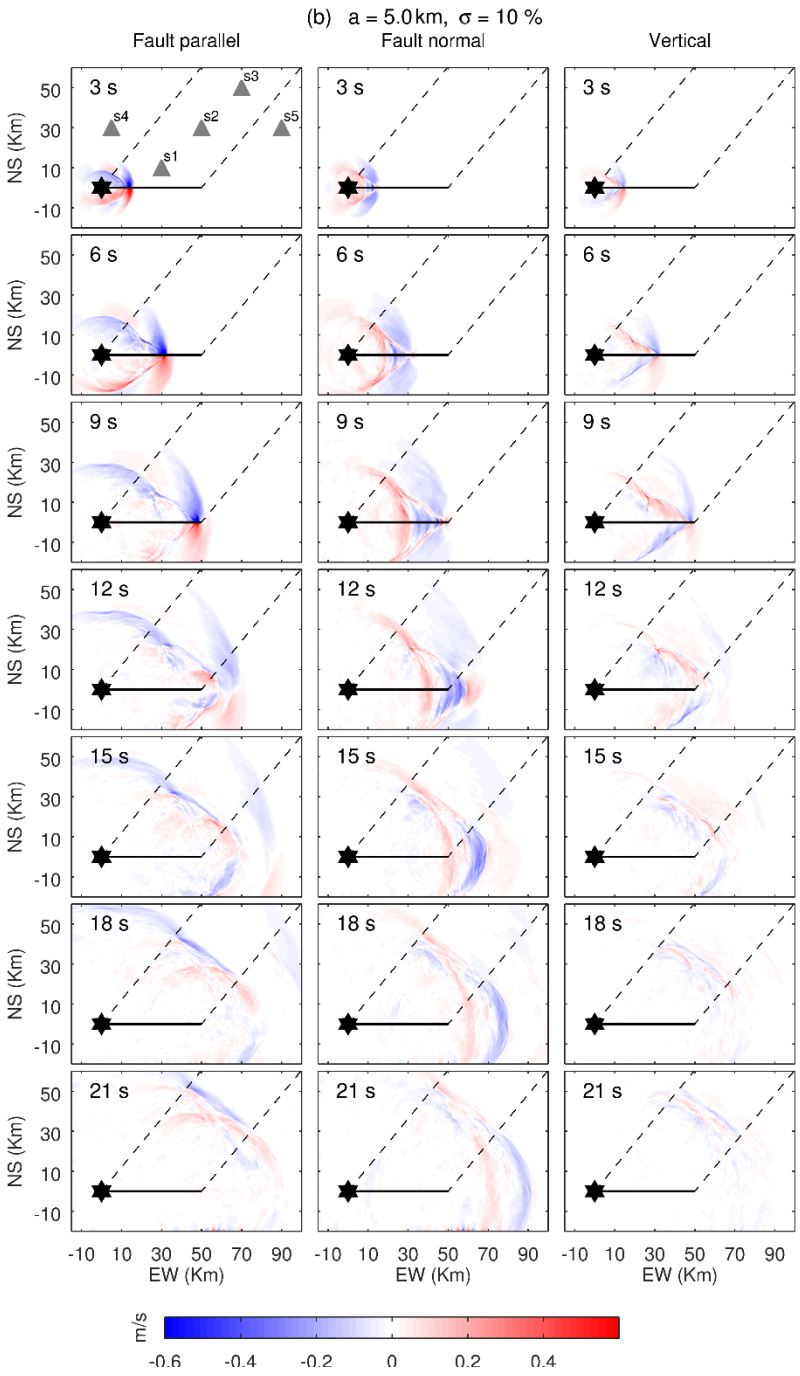

Figure S7: Snapshots in time of the velocity wavefield at the Earth-surface for three components of motion for media M1 (a = 5.0 km, σ = 5%) and M4 (a = 5.0 km, σ = 10%). As the Mach wave travels away from the fault, peak amplitudes decrease due to seismic scattering. Scattering effects, and hence amplitude reductions, are larger for medium with σ = 10%.

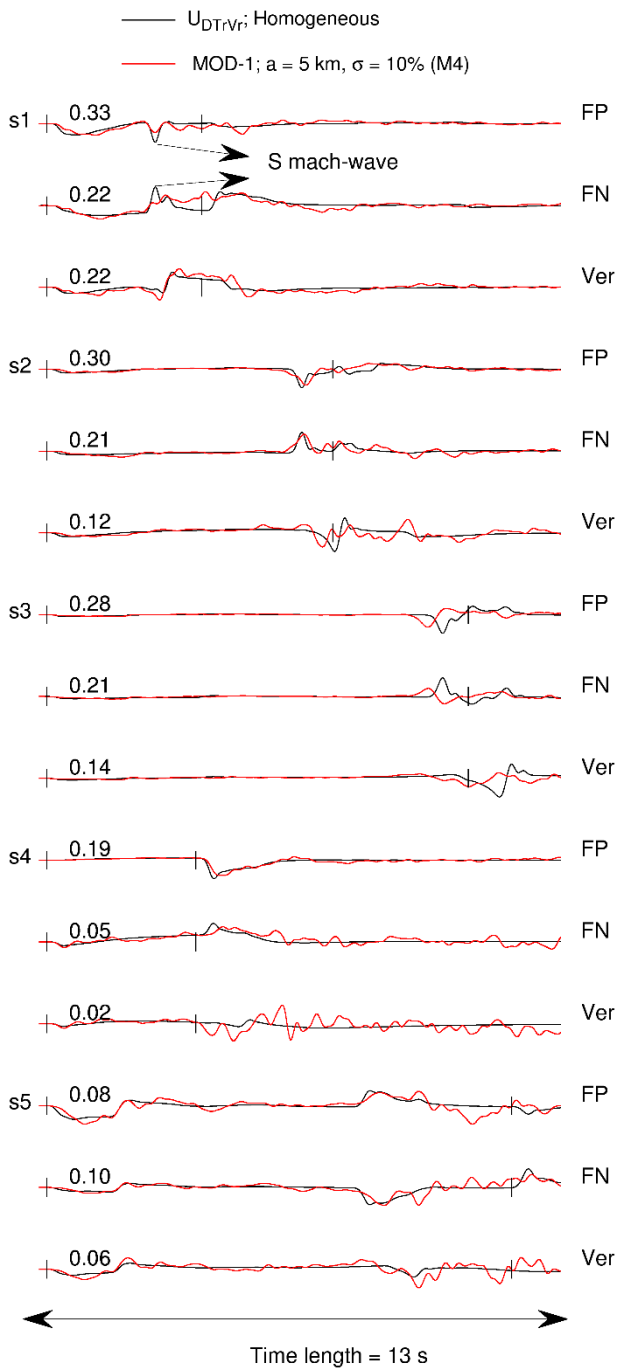

Figure S8: Ground velocity (m/s) for the fault-parallel (FP), fault-normal (FN) and Vertical (Ver) components, comparing MOD-1 in M4 to U_{DTrVr} in the homogeneous medium at five stations (s1 - s5, Figure 1-f). The theoretical P- and S-wave arrival times in the homogeneous medium are shown for reference. Waveforms are aligned according to the epicentral P-arrival time and normalized with respect to absolute maximum of two signals for a given component (indicated in upper left corner).

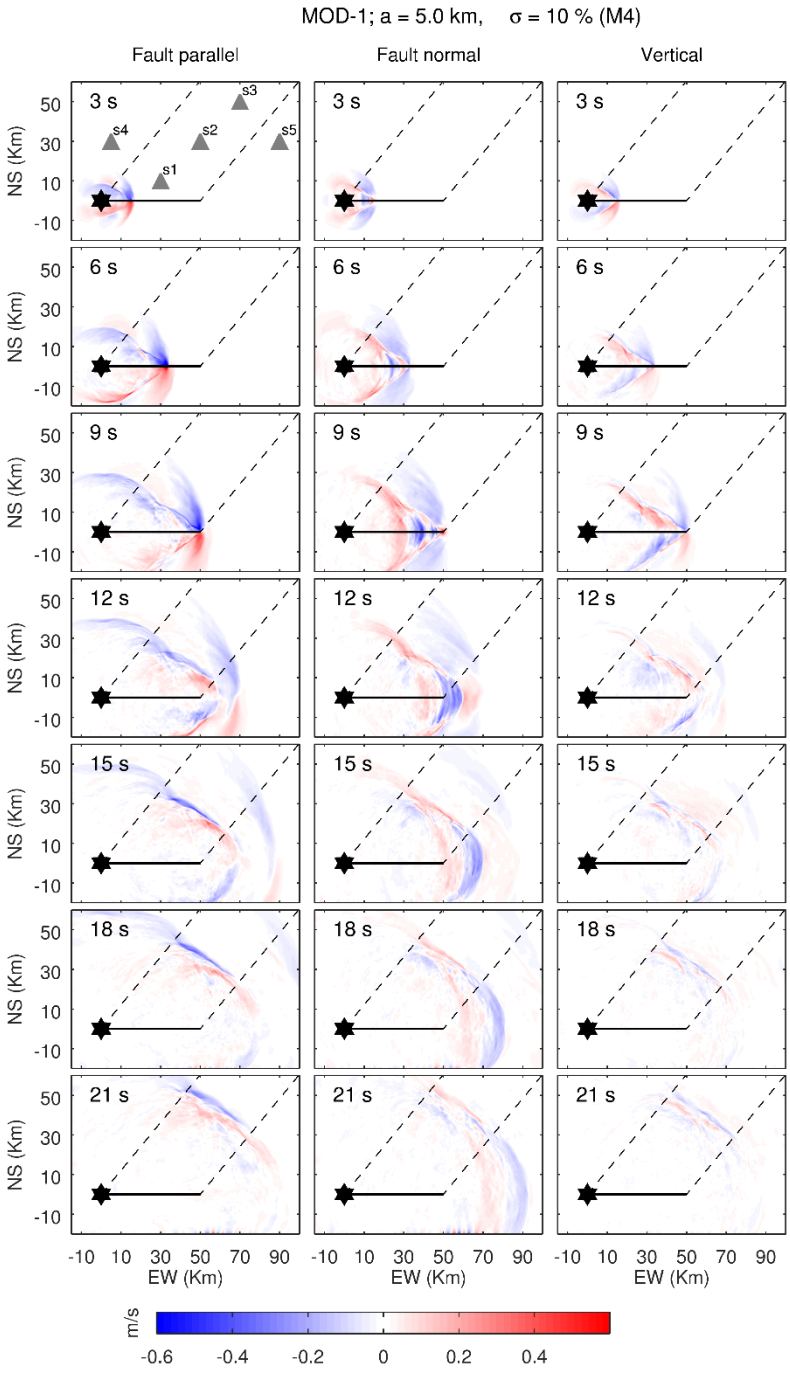

Figure S9: Snapshots in time of the velocity wavefield at the Earth-surface for the three components of motion for source model MOD-1 in M4. Rupture parameters heterogeneities of MOD-1 lower the Mach wave amplitudes, which are then further reduced by scattering as the Mach wave travels away from the fault.